Journal of chemical & engineering data

Article

Cite This: J. Chem. Eng. Data 2019, 64, 3755−3771

pubs.acs.org/jced

Molecular Simulations Probing the Thermophysical Properties of Homogeneously Stretched and Bubbly Water Systems

Jingyi L. Chen,[†] Bai Xue,[†] Krishnan Mahesh,[‡] and J. Ilja Siepmann*[,†,¶]

[†]Department of Chemistry and Chemical Theory Center, University of Minnesota, 207 Pleasant Street SE, Minneapolis, Minnesota 55455-0431, United States

[‡]Department of Aerospace Engineering and Mechanics, University of Minnesota, 110 Union Street SE, Minneapolis, Minnesota 55455-0153, United States

[¶]Department of Chemical Engineering and Materials Science, University of Minnesota, 421 Washington Avenue SE, Minneapolis, Minnesota 55455-0132, United States

Supporting Information

ABSTRACT: Molecular simulations in the canonical ensemble were performed to probe a variety of thermophysical properties of both homogeneously stretched and bubbly water systems at a temperature of 298 K. Two types of water models, the four-site TIP4P/2005 model and the coarse-grained single-site mW model, were investigated. Simulations for the computationally efficient mW model were carried out using cubic simulation boxes with linear dimensions of 4, 8, 16, and 32 nm, whereas 4, 6, and 8 nm boxes were considered for the TIP4P/2005 model. Various thermophysical properties, including pressure (P), potential energy (U), residual isochoric heat capacity ($C_{V,\mathrm{res}}$), viscosity (η), and self-diffusion coefficient (D_{self}), were calculated for densities ranging from 800 kg/m^3 to the saturated liquid density (ρ_{sat}). Following two simulation protocols starting either from a homogeneous configuration or from a heterogeneous configuration with a single spherical cavity, spinodal cavitation (SC) and bubble collapse (BC) points were located separately. This behavior of a fluid in a box of fixed volume is analogous to the hysteresis observed for adsorption−desorption isotherms of a subcritical fluid in a mesoporous adsorbent. As the system size is increased, both BC and SC points are shifted to larger densities. In terms of thermophysical properties, qualitatively similar trends are observed for the mW and TIP4P/2005 models. As the system approaches the SC point from ρ_{sat}, P decreases to a large negative value, U, $C_{V,\mathrm{res}}$, and η increase, and D_{self} decreases. Upon cavitation, the system undergoes a relaxation as signaled by step changes in these properties. In the heterogeneous (bubbly) region, a decrease in the density leads to relatively slower increases in P and U and a slow decrease in η, but $C_{V,\mathrm{res}}$ does not exhibit significant changes, whereas a significant decrease in D_{self} is observed only for the mW model and boxes larger than 8 nm. For the system sizes investigated here, the thermophysical properties at a given density cannot be simply estimated from a linear combination of the corresponding properties taken from the saturated liquid and vapor phases. For the bubbly phases, the Young−Laplace relation is found to hold well, whereas the Stokes−Einstein relation is not obeyed.

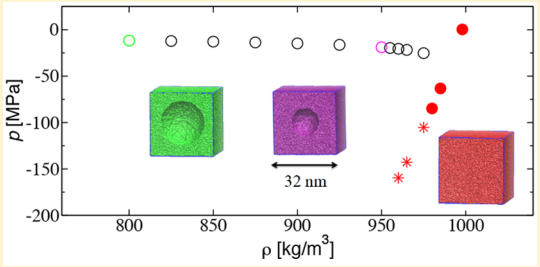

INTRODUCTION

Cavitation refers to the formation of vapor cavities inside a liquid when the pressure drops below the saturated vapor pressure. It is widely observed and is often undesirable. For example, around the blades of a working propeller, bubbles are formed due to localized low-pressure regions. The subsequent collapse of bubbles can generate strong shock waves or high local temperatures that can cause damage to the blades.[1] An image of sheet cavitation on a hydrofoil is shown in Figure 1. Understanding and predicting cavitating flows is inherently challenging due to the variety of phenomena involved that can span large temporal and spatial scales. Currently many of these phenomena are modeled empirically or are not included in the field of computational fluid dynamics (CFD), and much ongoing research is devoted to improving the underlying physical models and eliminating empiricism.[2,3]

Although molecular dynamics simulations can only access much smaller temporal and spatial scales compared to CFD, they can potentially be very useful because of the explicit consideration of the molecular nature of fluids and the ability to probe finite-size model system under conditions that are not stable for bulk systems. In addition, the scales of some physical phenomena involved in the cavitating flow, such as bubble nucleation and growth, are inherently compatible with molecular simulations. In fact, homogeneous bubble nucleation in liquid water has been explored using molecular simulations.[7−9]

Special Issue: FOMMS

Received: March 31, 2019
Accepted: May 1, 2019
Published: May 14, 2019

DOI: 10.1021/acs.jced.9b00284
J. Chem. Eng. Data 2019, 64, 3755−3771

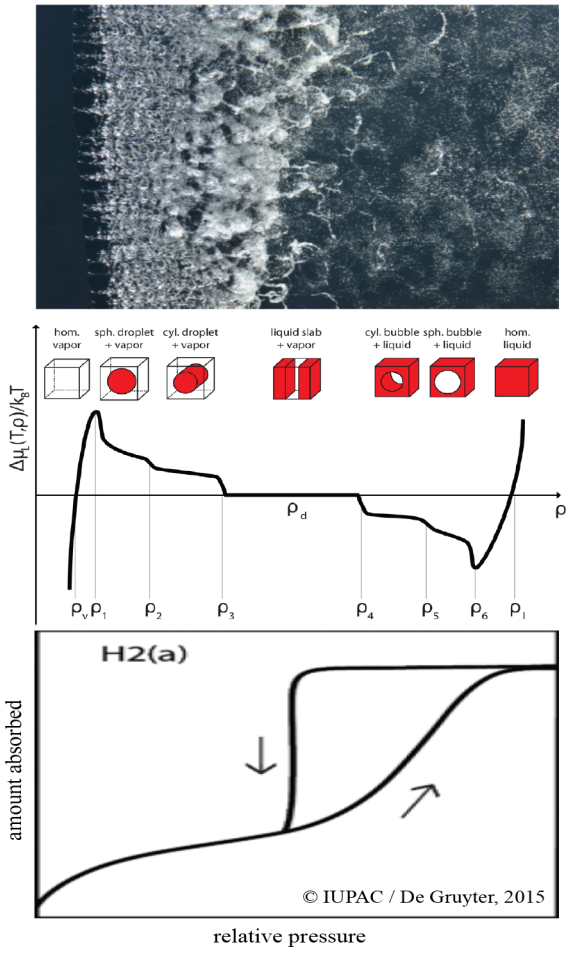

Figure 1. (Top) High-resolution photograph of sheet cavitation on a hydrofoil. Reprinted with permission from ref 4. (Middle) Chemical potential and morphology as a function of density for the LJ fluid. Figure reprinted with permission from ref 5. Copyright American Association of Physics Teachers. (Bottom) Type H2(a) hysteresis loop observed for an adsorption−desorption isotherm in a mesoporous adsorbent with delayed, but steep desorption due to caviatition-induced evaporation. Reprinted with permission from ref 6.

Molecular simulations can also be utilized to assess some of the underlying equations applied in CFD for predicting cavitating multiphase flow. For example, in the commonly used homogeneous mixture approach, liquid and vapor regions are assumed to have equal velocity and behave like a single compressible continuum in a given CFD cell (i.e., the vapor and liquid regions are assumed to form a homogeneous mixture within this cell).[10] In this approach, the governing equations describing the conservation laws are written for the homogeneous mixture, and an analytic or tabulated equation of state (EOS) for this mixture is needed for system closure.[11,12] In addition, a set of equations describing the properties of the mixture, such as viscosity, are often needed as well.[12,13] However, the mixture EOS and property equations utilized in practice are rarely validated through experiments for multiphase systems.[12] For example, a mixture EOS is usually chosen on the basis of its capability of reproducing the experimentally measured sound speed, yet available experimental data, though already sparse, are mostly concerned with liquid/gas mixtures, and reliable data for liquid/vapor mixtures probably do not exist.[14,15] Here, the term "vapor" refers to a phase that condenses to a liquid phase upon the increase of pressure at constant temperature (i.e., just water vapor), whereas a gas phase contains noncondensable species at this temperature (e.g., nitrogen or oxygen). Another example is the variety of equations that relate liquid/vapor mixture viscosity with bulk-phase viscosity and vapor-volume fraction.[16,17] These equations are mostly not derived directly from experimental viscosity data but estimated using experimental data for pressure drops of two-phase flow. In these cases, molecular simulation offers an alternative tool for assessing these equations and can potentially lead to better options.

In this work, molecular simulations in the canonical ensemble at T = 298 K were performed to probe a variety of thermophysical properties of neat water for densities ranging from the saturated liquid density (ρ_{sat}) to 800 kg/m^3 for periodic simulation boxes ranging from 4 to 32 nm. The lower bound at 800 kg/m^3 was chosen such that all inhomogeneous phases observed in the simulations have a single spherical cavity (denoted as bubbly water phase), rather than a cylindrical cavity or even a slab structure (see Figure 1). Binder et al.[5] have previously studied the phase behavior of the Lennard-Jones (LJ) fluid for densities ranging from below the saturated vapor density to above the satured liquid density for a periodic system with fixed linear dimension. As illustrated in Figure 1, the LJ fluid undergoes a transition from the homogeneous liquid phase to the bubbly phase as the density is reduced from ρ_l to below ρ_6. In our work, a similar phase behavior was observed for water as well. By following two different simulation protocols, where one starts with a homogeneously stretched configuration (protocol 1), while the other starts with a spherical cavity (protocol 2), we were able to locate the spinodal cavitation (SC) and bubble collapse (BC) points separately. At these points, the free energy barrier for transition to a more stable phase becomes sufficiently small so that this phase transition occurs rapidly in the early part of the simulation. The differences observed between simulations utilizing protocols 1 (desorption) and 2 (adsorption) are analogous to the hysteresis loops observed for adsorption−desorption isotherms in mesoporous adsorbents.[6] In particular, type H2(a) hysteresis can be attributed to a system with wetting pore walls and delayed desorption due to cavitation-induced evaporation[6] (see Figure 1). Similarly, the formation of a bubble can be delayed for simulations in the canonical ensemble due to the free energy barrier for bubble nucleation; that is, as for the desorption branch, the metastable stretched liquid phase can persist. On the other hand, the vapor−liquid interface of the bubble initially present using protocol 2 acts like a wetting wall, the bubble shrinks as the overall density is increased and then disappears when the homogeneously stretched liquid state is lower in free energy than the bubbly state. It should be noted that the hysteresis loops observed in adsorption−desorption isotherms are experimentally reproducible and "permanent", that is, increasing the time scale for the sorption measurements from hours to months leads only to negligible changes in the hysteresis loop. Considering the time scale of flow experiments and CFD simulations, it is likely that, in the absence of seeds or surfaces, bubbles form through spinodal decomposition instead of homogeneous nucleation. In this case, the metastable homogeneous states observed with protocol 1 provide important information for the modeling of multiphase flow.

The thermophysical properties investigated in this work include pressure (P), potential energy (U), residual isochoric

DOI: 10.1021/acs.jced.9b00284
J. Chem. Eng. Data 2019, 64, 3755−3771

heat capacity ($C_{V,res}$), viscosity (η), and diffusion coefficient (D_{self}). Previous molecular simulation studies have investigated the thermophysical properties of stretched homogeneous water at similar conditions,[18−21] and comparisons are made here to these earlier studies. To our knowledge, the thermophysical properties of two-phase bubbly water have not been investigated previously. Since the spatial scale of the cells involved in CFD is usually micrometers or larger and, hence, orders of magnitude larger than those amenable to molecular simulation, attention needs to be given to finite-size effects. For simulations in the canonical ensemble, such as the current work, system-size effects refer to changes of observables with system size (increasing linear dimension of the simulation box) at fixed system density. However, for inhomogeneous bubbly water systems, an increase in system size at fixed density necessarily also requires a corresponding change in bubble radius and volume, whereas the bubble volume fraction is less affected. The results obtained from molecular simulations are compared with some of the available equations utilized in CFD. Analytic equations fitted to simulation data are proposed for describing the properties of the bubbly water state if possible.

MODELS AND SIMULATION DETAILS

Force Fields. Two types of water models were used in this work (see Table 1). The first one is the rigid TIP4P/2005 water model,[22] which consists of a single LJ site on the position of the oxygen nucleus, two equal partial charges on the position of the hydrogen nuclei, and a negative partial charge located at an off-site location along the H−O−H bisector to keep the molecule neutral. The intermolecular interactions are described by pairwise additive LJ 12−6 and Coulomb potentials:

Table 1. Chemical Compounds, Suppliers, and Purity

chemical name	molecular formula	CASRN	supplier	purity	analysis method
water	H_2O	7732-18-5	mW	100.0%	input file
water	H_2O	7732-18-5	TIP4P/2005	100.0%	input file

$$u_{ij}(r_{ij}) = 4\varepsilon_{ij}\left[\left(\frac{\sigma_{ij}}{r_{ij}}\right)^{12} - \left(\frac{\sigma_{ij}}{r_{ij}}\right)^{6}\right] + \frac{q_i q_j}{4\pi\epsilon_0 r_{ij}} \quad (1)$$

where r_{ij}, ϵ_{ij}, σ_{ij}, q_i, q_j, and ϵ_0 are the distance between interaction sites i and j, the LJ well depth, the LJ diameter, the partial charges on interaction sites i and j, and the permittivity of vacuum, respectively. In our simulations, periodic boundary conditions were applied to cubic simulation boxes in all three dimensions. LJ interactions were truncated at a distance r_{cut} = 1.40 nm. Since the bubbly water systems are inhomogeneous, the use of analytical tail corrections for LJ energy and pressure that assume a uniform pair distribution beyond the truncation distance would be inappropriate. Therefore, for consistency, no LJ tail corrections were applied throughout simulations and the same r_{cut} value is used for all system sizes. In the development of the TIP4P/2005 water model,[22] the LJ potential was truncated at 0.85 nm and tail corrections were employed. Thus, the larger r_{cut} at 1.40 nm used here mitigates the truncation error. To compute charge−charge interactions under periodic boundary conditions, the Ewald summation method[23,24] with a screening parameter $\kappa = \pi/r_{cut}$ and an upper bound of the reciprocal space summation at $K_{max} = \text{int}(\kappa L) + 1$ was utilized for Monte Carlo simulations, whereas the particle−particle particle−mesh Ewald summation technique[25,26] with a relative force error of 10^{-5} was utilized for molecular dynamics simulations.[25,27] The real-space site−site electrostatic interactions were truncated at r_{cut} as well.

The other water model utilized in this work is the coarse-grained mW water model[28] where each water molecule is represented by a single interaction site. In addition to a two-body interaction term, this water model also introduces a three-body interaction term favoring the tetrahedral packing of water molecules in the condensed phase. The potential takes the form

$$U = \sum_i \sum_{j>i} \phi_2(r_{ij}) + \sum_i \sum_{j\neq i} \sum_{k>j} \phi_3(r_{ij}, r_{ik}, \theta_{ijk}) \quad (2)$$

$$\phi_2(r_{ij}) = A\varepsilon\left[B\left(\frac{\sigma}{r_{ij}}\right)^m - \left(\frac{\sigma}{r_{ij}}\right)^n\right]\exp\left(\frac{\sigma}{r_{ij} - a\sigma}\right) \quad (3)$$

$$\phi_3(r_{ij}, r_{ik}, \theta) = \lambda\varepsilon(\cos\theta - \cos\theta_0)^2 \exp\left(\frac{\gamma\sigma}{r_{ij} - a\sigma}\right)\exp\left(\frac{\gamma\sigma}{r_{ik} - a\sigma}\right) \quad (4)$$

where A = 7.049556277, B = 0.6022245584, m = 4, n = 0, γ = 1.2, a = 1.8, θ_0 = 109.47°, λ = 23.15, ϵ = 6.189 kcal/mol, and σ = 0.23925 nm. In this model, both two-body and three-body interaction terms become negligible as pair distance approaches $a\sigma$ = 0.43065 nm. Owing to this short-ranged nature and fewer interaction sites per molecule, simulations typically gain at least 2 orders of magnitude in efficiency compared with that of the TIP4P/2005 water model, thus allowing for much larger system sizes.

Monte Carlo Simulations. Isochoric−isothermal (NVT) Gibbs ensemble Monte Carlo (GEMC) simulations[29,30] were performed using the Monte Carlo for Complex Chemical Systems-Minnesota (MCCCS-MN) software[31] developed in house to determine the vapor−liquid equilibrium (VLE) properties (densities of both phases and vapor pressure) at T = 298 K. These simulations used two boxes to represent liquid and vapor phases. The total number of molecules N was set to 2000. To ensure a sufficient number of molecules in the vapor box, the initial box lengths for the liquid and vapor boxes were set to 4 and 100 nm, respectively. Because of the large vapor box utilized, r_{cut} for the vapor box was set to 40 nm instead of 1.4 nm to reduce computational cost for the reciprocal-space part of the Ewald sum. For each simulation, the equilibration period consisted of at least 50 000 Monte Carlo cycles (MCCs; one MCC consists of N randomly selected moves), and the production period consisted of 100 000 MCCs. Statistical uncertainties were estimated from the standard error of the mean at 95% confidence interval obtained from production periods of eight independent simulations.

For the TIP4P/2005 water model, the phase space was sampled via translational moves,[32] rotational moves,[33] volume exchange moves,[30] and particle transfer moves between phases using the dual cutoff configurational-bias Monte Carlo algorithm[34,35] with optimized control parameters and growth protocol.[36] The maximum displacements for translational, rotational, and volume moves were adjusted during equilibration to yield acceptance ratios of approximately 40%. To

DOI: 10.1021/acs.jced.9b00284
J. Chem. Eng. Data 2019, 64, 3755−3771

increase sampling efficiency and also to avoid unphysical "fused" configurations where a positively charged interaction site of one water molecule is nearly colocated with the negatively charged site of another water molecule, a hard-sphere potential with r_{HS} = 0.12 nm was applied for all site−site interactions. For the mW water model, phase space was sampled via translational, volume exchange, and particle transfer moves. A hard-sphere potential with r_{HS} = 0.05 nm was utilized as well to improve sampling efficiency and to avoid underflow errors in the calculation of Boltzmann weights.

Molecular Dynamics Simulations. Molecular dynamics simulations were carried out using the LAMMPS software package.[37] All simulations were performed in the *NVT* ensemble. The time step was set to 1 or 5 fs for the TIP4P/2005 or mW water models, respectively. The temperature was maintained at 298 K using the Nose−Hoover thermostat,[38] and its relaxation time was set to 100 fs. For the rigid TIP4P/2005 water model, the O−H bonds and H−O−H angle were constrained using the SHAKE algorithm.[39]

Simulations were first performed to calculate the surface tension for the TIP4P/2005 and mW water models. Following the Kirkwood and Buff definition,[40] the surface tension was calculated from the ensemble averages of the normal and tangential components of the pressure tensor. The simulation procedure consisted of two steps. First, a stable liquid configuration was obtained by performing simulations in the *NVT* ensemble with N = 1024 and a cubic box of length L = 3 nm. Then the simulation box was elongated in the z dimension to L_z = 10 nm, and equilibration was continued for at least 0.5 ns. Statistics were gathered from production periods of 2 ns.

Next, simulations were performed to probe a variety of thermophysical properties of both the homogeneously stretched liquid and the bubbly water phase. The box lengths (L) studied were 4, 8, 16, and 32 nm for the mW water model (and these simulations are designated here as mW-4, mW-8, mW-16, and mW-32, respectively), containing up to 1 092 850 molecules in the largest system, and 4, 6, and 8 nm for the TIP4P/2005 model (desginated as TIP4P/2005-4, TIP4P/2005-6, and TIP4P/2005-8, respectively). For each box size, densities ranging from 800 kg/m^3 to ρ_{sat} were explored. The densities and number of molecules for all the systems studied here are provided in Table S1.

Two simulation protocols were utilized. In protocol 1, a homogeneous configuration was used as the starting point. The initial structure for the mW water model was generated randomly using LAMMPS. Then the potential energy was minimized by adjusting the coordinates of the molecules iteratively for a maximum of 1000 steps. For the TIP4P/2005 water model, the initial structure was generated using the Packmol program with a tolerance distance of 0.2 nm.[41,42] After that, for both water models, the system underwent a brief melting and a subsequent cooling stage. In protocol 2, the initial heterogeneous configuration was generated such that all molecules were placed outside of a sphere with its center located at the center of the simulation box and a radius ranging from 0.5 to 1.5 nm. For the single-site mW water model, this was achieved with built-in commands in LAMMPS, while Packmol was utilized for the TIP4P/2005 water model. Next, a spherical wall was created in LAMMPS, that interacts with the water molecules through a 12−6 LJ potential and prevents any molecules from entering the cavity during the pre-equlibration period. After a short melting and subsequent cooling stage, the wall was removed and the system was allowed to equilibrate.

For the mW-4, mW-8, and mW-16 systems, statistics were collected from a production period of 20 ns. For the mW-32 system, statistics were collected from five independent runs, each consisting of a production period of 4 ns. For the TIP4P/2005-4 and TIP4P/2005-6 systems, statistics were collected from a production period of 4 ns. For the TIP4P/2005-8 system, statistics were collected from five independent runs, each consisting of 1.6 ns. For both water models, the independent runs were created by using different random number seeds for generating initial structures and velocity distributions. A detailed description of how the uncertainties were estimated for the various quantities is given in the following sections.

Bubble Volume and Sphericity. For bubbly water systems, the bubble volume for a given configuration along the trajectory was determined as follows. First, Stillinger's cluster criterion[43] was utilized to calculate the number of nearest neighbors of each water molecule where two molecules are considered nearest neighbors if their distance (oxygen−oxygen for TIP4P/2005 and site−site for mW) is less or equal to 0.33 nm; a distance that is approximately the position of the first minimum in the O−O radial distribution function for the saturated liquid phase of the TIP4P/2005 model. If a molecule has two or more nearest neighbors, it is then considered to be liquid-like, otherwise it is counted as vapor-like. Next, a three-dimensional grid with a cell mesh of $(0.2\ \text{nm})^3$ was imposed onto the simulation box. If a cell contains a liquid-like water molecule or its center falls within 0.33 nm of at least two liquid-like molecules, then it is considered to be liquid-like, and the remaining cells are defined as vapor-like. Finally, a cluster analysis was performed considering only the vapor-like cells, and two cells are part of the same cluster when they share at least one corner. The detected number of clusters is sometimes larger than one for a single configuration due to the existence of very small voids being formed by thermal fluctuations inside the liquid region. Only the largest cluster, the size of which is always significantly larger than any of the transient liquid voids, is taken as the bubble and used to calculate the bubble volume, V_{cell}, from its number of cells. Since this analysis is based on individual configurations, the statistical uncertainty in the bubble volume fraction is reported here as the standard deviation obtained from the values for individual configurations. The cell method for bubble detection described here is computationally more efficient than the V- and M-methods proposed by González et al.,[8] and a simpler method is justified because the current work deals with much larger systems (requiring a more efficient method) and much larger bubbles (being less sensitive to the method for bubble detection).

To characterize bubble sphericity, the gyration tensor was calculated as

DOI: 10.1021/acs.jced.9b00284
J. Chem. Eng. Data 2019, 64, 3755−3771

Table 2. Calculated and Experimental Orthobaric Liquid Density (ρ_{liq}), Vapor Density (ρ_{vap}), Saturated Vapor Pressure (P_{sat}), Enthalpy of Vaporization (ΔH_{vap}), Liquid−Vapor Surface Tension at Saturation (γ), and Their Uncertainties (u) at T = 298 K[a]

		TIP4P/2005		mW		
property		value	u	value	u	expt[52]
ρ_{liq}	[kg/m^3]	994.4	1.3	997.66	0.19	997.04
ρ_{vap}	[g/m^3]	5.39	0.13	0.3561	0.0051	22.881
P_{sat}	[kPa]	0.739	0.017	0.04853	0.00078	3.1
ΔH_{vap}	[kJ/mol]	50.164	0.042	44.432	0.062	44.01
γ	[mN/m]	65.9	1.7	65.47	0.24	71.995

[a]Statistical uncertainties were estimated from the standard error of the mean at 95% confidence interval obtained from production periods of eight independent simulations.

$$S = \frac{1}{N_{vap}} \begin{bmatrix} \sum_i (x_i - x_C)^2 & \sum_i (x_i - x_C)(y_i - y_C) & \sum_i (x_i - x_C)(z_i - z_C) \\ \sum_i (y_i - y_C)(x_i - x_C) & \sum_i (x_i - x_C)^2 & \sum_i (y_i - y_C)(z_i - z_C) \\ \sum_i (z_i - z_C)(x_i - x_C) & \sum_i (z_i - z_C)(y_i - y_C) & \sum_i (z_i - z_C)^2 \end{bmatrix} \quad (5)$$

where x_C, y_C, and z_C give the position of the center of mass of the bubble. The summation runs only over the vapor-like cells belonging to the bubble, where N_{vap} is the number of these cells. Then, the gyration tensor is diagonalized, and its three eigenvalues λ_1, λ_2, and λ_3 are obtained. The relative shape anisotropy is defined as[44]

$$\kappa^2 = 1 - 3\frac{\lambda_1\lambda_2 + \lambda_2\lambda_3 + \lambda_1\lambda_3}{(\lambda_1 + \lambda_2 + \lambda_3)^2} \quad (6)$$

κ^2 is bounded between 0 and 1 corresponding to a spherically symmetric shape and a linear shape, respectively.

Thermophysical Properties. The pressure of the system was calculated based on the virial theorem of Clausius:[45,46]

$$p = \rho k_B \langle T \rangle + \frac{1}{3V} \left\langle \sum_i \mathbf{r}_i \cdot \mathbf{f}_i \right\rangle \quad (7)$$

where k_B is the Boltzmann constant, ρ, V, and T are the number density of molecules, volume, and absolute temperature of the system, respectively. For the molecular dynamics simulations, T is calculated based on the kinetic energy of the system. $\mathbf{r}_i$ and $\mathbf{f}_i$ are the position vector and the force exerted on atom i. The angular brackets in the first and second terms denote time averages (or, only for the second term, an ensemble average for the Monte Carlo simulations) of temperature and the internal virial, respectively.

The isochoric heat capacity can be split into ideal and residual parts:

$$C_V(T, V) = C_{V,ideal}(T) + C_{V,res}(T, V) \quad (8)$$

where $C_{V,ideal}$ is a property of a collection of isolated molecules and can be determined from calorimetric measurements or the molecular partition function with input either from spectroscopic data or quantum-mechanical calculations.[47,48] $C_{V,ideal}$ includes the kinetic contributions. The residual part is determined from fluctuations of the intermolecular potential energy of the system. However, for the rigid TIP4P/2005 and the single-site mW models, there are no intramolecular contributions. Therefore, the potential energy (U) of the system can be directly used:

$$C_{V,res} = \frac{\langle U^2 \rangle - \langle U \rangle^2}{k_B T^2} \quad (9)$$

The shear viscosity was calculated using the Green−Kubo approach,[49]

$$\eta = \frac{V}{k_B T} \int_0^\infty dt \langle P_{\alpha\beta}(0) P_{\alpha\beta}(t) \rangle \quad (10)$$

where $P_{\alpha\beta}(0)$ and $P_{\alpha\beta}(t)$ are the off-diagonal components of the pressure tensor at time 0 and t, and are averaged over three components P_{xy}, P_{yz}, and P_{xz}. The viscosity calculated this way for an inhomogeneous system is the averaged value over the entire box.[50] Since the autocorrelation function in the above equation often diverges due to accumulation of noise at long time, a time decomposition method was utilized in this work.[51] To make sure the viscosity value has converged, the integral was truncated at 1.0 ps for the mW model and 3.0 ps for the TIP4P/2005 model. The justification for these choices of the time cutoff is presented in Figure S1.

For the estimation of the statistical uncertainties for pressure, potential energy, residual isochoric heat capacity, and shear viscosity, the total production period of each simulation was divided into eight blocks and the block means were calculated. The uncertainties were estimated as the standard error of the mean at 95% confidence interval.

Finally, the diffusion coefficient was obtained through the mean squared displacement (MSD) of the center of mass of molecules and the Einstein relationship,[24]

$$D = \frac{1}{6t} \left\langle \frac{1}{N} \sum_{i=1}^{N} [\mathbf{r}_i(t) - \mathbf{r}_i(0)]^2 \right\rangle \quad (11)$$

where $\mathbf{r}_i(t)$ and $\mathbf{r}_i(0)$ are the position vectors of the center of mass of molecule i at time t and 0. To calculate the uncertainties for the diffusion coefficient, each trajectory was divided into five blocks. For the largest system, mW-32 and TIP4P/2005-8, each independent simulation was considered

DOI: 10.1021/acs.jced.9b00284
J. Chem. Eng. Data 2019, 64, 3755−3771

as one block. The lengths of each block (4 ns for the mW-4, mW-8, and mW-16 systems, 0.8 ns for the TIP4P/2005-4 and TIP4P/2005-6 systems, and 1.6 ns for the TIP4P/2005-8 system) were chosen to be sufficiently long such that, on average, molecules have diffused more than half of the box length. The diffusion coefficient for the mW-32 system was not calculated because, although a linear region is present in the MSD plot, the trajectory length of 4 ns is insufficient to reach an MSD value of $(16\ \text{nm})^2$. The diffusion coefficient for each block was obtained from the slope of the least-squares linear fitting line between MSD and time (where the first 10% and last 10% of data points were thrown out in the fitting to avoid the initial ballistic region and the relatively poor statistics at the end). An example MSD plot obtained from the five blocks for the TIP4P/2005-8 system is shown in Figure S2. The statistical uncertainties provided are the standard error of the mean at 95% confidence interval obtained from the five blocks.

RESULTS AND DISCUSSION

VLE properties and Surface Tension. The predicted VLE properties and surface tension at $T = 298$ K are listed in Table 2. The liquid-phase density at saturation for both types of water models agrees well with experiment. Both water models predict a surface tension value which is approximately 7% smaller than the experimental value, and the values obtained here are consistent with previous simulation results.[28,53] However, in terms of vapor pressure and vapor density at saturation, both water models underestimate by a significant amount. The TIP4P/2005 water model yields predictions that are a factor of 4.2 smaller than the experimental values, which is due to an overestimation of the enthalpy of vaporization when a polarization correction is not applied.[22,54] The mW water model underestimates them by a factor of 64. Factorovich et al.[55] also computed the vapor pressure for the mW water model at $T = 298$ K using both GEMC and grand canonical molecular dynamics (GCMD) simulations and reported values of 45.8 and 48.6 Pa, respectively. Their GCMD value is more consistent with the value obtained here from a GEMC simulation. Interestingly, the mW model yields a fairly accurate value for the enthalpy of vaporization[28] and, hence, its significant underestimation of the saturated vapor pressure is caused by an underestimation of the entropy gain upon vaporization. The fact that a model can yield a very accurate liquid density and a fairly accurate surface tension (and, for the mW model, also enthalpy of vaporization), but fail dramatically for the saturated vapor pressure, indicates that the former two properties are not sufficient for force field development.

Spinodal Cavitation and Bubble Collapse Points. An important observation for systems with $L \geq 6$ nm is that the transition point between the homogeneously stretched water phase and the bubbly water phase occurs at a lower density for the set of simulations starting from a homogeneous configuration, where the system has to overcome the nucleation free energy barrier for bubble formation, compared to those simulations starting with a pre-existing cavity, where no (or only a small) free energy barrier for bubble collapse is present. These two transition processes and their associated densities are denoted as spinodal cavitation (SC) and bubble collapse (BC), respectively. It should be noted that, for the finite-size systems investigated here, the BC process occurs with a downward jump in pressure and leads to a homogeneous phase with a negative pressure; that is, it is distinct from the vapor−liquid binodal point that denotes the coexistence of two stable macroscopic phases with positive pressure. While analyzing the bubble volume fraction, we observed that when the SC density is crossed, there is always a significant jump of the volume fraction of the largest void/bubble from less than 0.2% due to small transient liquid voids in the homogeneously stretched water phase to more than 1% when a bubble is formed. Similarly, for simulations using protocol (2), we find that there is a certain minimum bubble size that can be observed in the simulations. This minimum bubble size found in the simulations increases with system size and the bubble volume fraction is always significantly larger than 1%. We surmise that at the BC point, the free energy of the bubbly phase with this minimum bubble size is equal to that of the homogeneously stretched phase. Any reduction of the bubble size beyond this limit cannot be observed because this state would have a free energy higher than the homogeneously stretched phase at the same density; i.e., the system prefers homogeneous stretching (with a more negative pressure) over affording an interface (and less stretching of the liquid region). Since larger systems have to stretch by a smaller relative amount to consume a given bubble volume, the minimum observable bubble size increases with increasing system size.

Therefore, in this work, a system is considered to be a bubbly water phase only when the bubble volume fraction is larger than 1%. Similar significant and discontinuous changes were also observed in other thermophysical properties near the same transition points and will be discussed in the following sections.

For the two smallest systems (mW-4 and TIP4P/2005-4) that contain about 2000 molecules, distinct SC and BC points were not observed with a density resolution of 5 kg/m^3. At the intermediate density (930 kg/m^3 for mW-4 and 880 kg/m^3 for TIP4P/2005-4) between homogeneously stretched and bubbly water phases, the systems were found to alternate between homogeneous and inhomogeneous configurations (as defined by the 1% threshold in the bubble volume fraction) causing large fluctuations also in other observables. Owing to the large fluctuations arising from the bimodal distributions, thermophysical properties at these two state points are not reported here.

The Helmholtz free energies as a function of the largest void/bubble volume for the mw-4 and TIP4P/2005-4 systems at these state points are shown in Figure S3. The barrier separating the two states is found to be 10−12 kJ/mol (4−5 RT) and its location at $V \approx 0.6\ \text{nm}^3$ is aligned with the 1% threshold used here to separate the two states. Menzl et al.[9] have used simulations in the isobaric−isothermal ensemble at $N = 2000$ and $T = 296.4$ K with enhanced sampling techniques to probe the cavitation of TIP4P/2005 water under tension. Our canonical ensemble simulations for TIP4P/2005-4 correspond to a similar system size, and our observation of the SC point falling into a pressure range from −190 to −200 MPa is consistent with the data of Menzl et al. that show nucleation free energy barriers of 30 and 20 RT at $P = -150$ and −165 MPa, respectively.

The specific densities of the SC and BC points are plotted as a function of an inverse linear box dimension in Figure 2. Owing to the finite resolution of the density grid (increments of 5 kg/m^3), the exact values of the spinodal and binodal points are not known, and hence, they are reported here as the average of the specific densities just below and just above of

DOI: 10.1021/acs.jced.9b00284
J. Chem. Eng. Data 2019, 64, 3755−3771

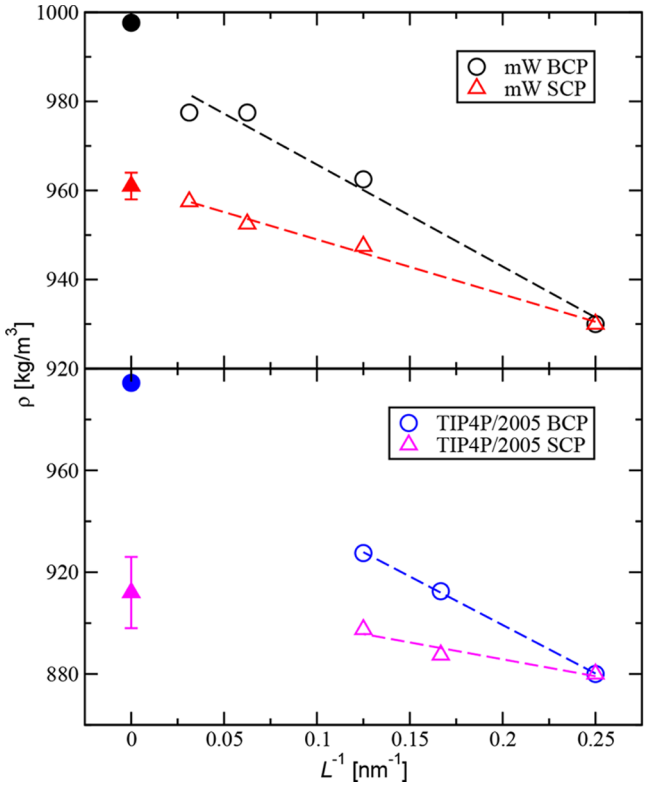

Figure 2. Specific densities of the SC and BC points for the mW and TIP4P/2005 systems as a function of inverse linear box dimension. The dashed lines indicate linear fits. The filled circles and triangles denote ρ_{liq} and the estimate of the SC density for the thermodynamic limit.

these points for $L \geq 6$ nm or as the density leading to large fluctuations in the bubble volume fraction for mW-4 and TIP4P/2005-4. González et al.[56] have previously used simulations in the canonical ensemble (N = 500) to estimate the vapor−liquid spinodal line for the TIP4P/2005 model, and from their data, a value of 850 kg/m^3 at T = 298 K can be deduced. In comparison, we find a value of 880 kg/m^3 for TIP4P/2005-4 that contains about 3.8 times more molecules (i.e., 1.6 times larger in linear dimension).

Another observation from Figure 2 is that, as system size increases, both SC and BC points shift to larger densities (except that mW-16 and mW-32 yield the same binodal density due to the finite grid resolution). This behavior is consistent with the system size effects found by Binder et al.[5] for the LJ fluid and also with the upward shift in the position of the hysteresis loop for adsorbents with larger mesopores.[6] Upon further increase in the system size, the BC point would move toward the saturated liquid density (i.e., the true binodal point), but the density domain for stable spherical bubbles also diminishes. In the thermodynamic limit, only the slab configuration with planar interfaces is stable at densities below the saturated liquid density (see Figure 1).[5] From extrapolation of our data for the SC points of the finite systems, we estimate spinodal densities of 912 ± 14 and 961 ± 3 kg/m^3 for the TIP4P/2005 and mW models, respectively, in the thermodynamic limit.

For the systems with $L \geq 6$ nm, the simulations started from a homogeneous configuration at densities below the BC point but above the SC point are metastable. The definition of a metastable state inherently involves time.[57] In the present simulations, we found that all simulations in the metastable region remained in a homogeneously stretched state throughout the entire simulation trajectories, and the same holds for the five independent simulations for largest system size (mW-32 and TIP4P/2005-8). The production periods for the mW-8, mW-16, mW-32, TIP4P/2005-6, and TIP4P/2005-8 systems were 20, 20, 4, 4, and 1.6 ns, respectively, with the equilibration periods being of various lengths but generally of the same order of magnitude as the production periods. Clearly, the nucleation free energy barrier increases rapidly for densities just above the spinodal point, so that nucleation does not occur in our unbiased simulations. This is analogous to the observation that increasing the observation time does not lead to a significant upward shift in the pressure of the desorption onset for the type H2(a) hysteresis loop (see Figure 1).[6] The Helmholtz free energies as a function of the volume of the largest void/bubble for the mW-8 and TIP4P/2005-8 systems are shown in Figure S4. The unbiased simulations used here only allow for observation of states with relative free energies less than 20 kJ/mol (8 RT). Extrapolating the free energy profiles for the metastable homogeneously stretched systems with the lowest density (i.e., closest to the SC point) yields a nucleation free energy barrier of 25 and 35 kJ/mol (10 and 14 RT) for TIP4P/2005-8 and mW-8, respectively. For both systems, the steepness of the free energy profiles increases rapidly with increasing system density. The estimate for the free energy barrier for TIP4P/2005-8 with N = 15398 and P = −168 MPa is considerably smaller than the 20 RT reported by Menzl et al.[9] for N = 2000 and P = −165 MPa; thus, finite-size effects are significant for the nucleation barrier for which smaller system sizes lead to larger barriers and a lower density for the SC point.

For the bubbly phases, the width of the free energy wells remains remarkably constant even as the BC density is approached; that is, we do not observe a significant change in curvature of the free energy profile that would hint at the emergence of the homogeneously stretched phase. On the other hand, the simulations using protocol (2) for the system density just above the BC point indicate that there is no thermodynamic barrier for the collapse.

Bubble Volume and Sphericity. The calculated bubble volume fraction (α) versus system density for all bubbly water phases is plotted in Figure 3 (numerical data are provided in Tables S2−S15). The line predicted by the simple analytic equation, $\rho_{mix} = (1 - \alpha)\rho_{liq} + \alpha\rho_{vap}$ is also shown in Figure 3 for comparison, where ρ_{liq} and ρ_{vap} are the experimental liquid and vapor coexistence densities. This analytic equation, which ignores any surface and pressure effects, is commonly utilized in predicting multiphase flow in CFD.[12]

As shown in Figure 3, α at a specific value of ρ is influenced by both system size and choice of water model. As the system size increases, the line predicted by the simulations for both the mW and TIP4P/2005 model is shifting to higher α values, that is, approaching the prediction of the analytic equation. For the same system size, the α values for the TIP4P/2005 water model fall below those for the mW water model, and the lines for the TIP4P/2005 model have a slightly steeper slope. Given the magnitude of the differences between the simulation data and the analytic equation and also the presence of finite-size effects, it is clear that the deviations cannot be attributed to differences in ρ_{liq} for the bulk systems (see Table 2). Further simplifying the analytic equation by dropping the vapor term because ρ_{vap} is orders of magnitude smaller than ρ_{liq} (by factors

DOI: 10.1021/acs.jced.9b00284
J. Chem. Eng. Data 2019, 64, 3755−3771

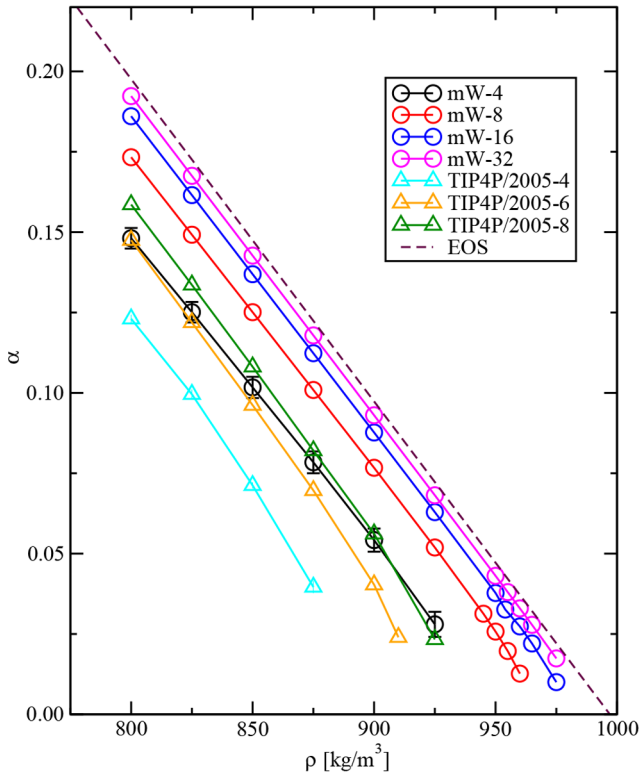

Figure 3. Bubble volume fraction (α) versus system density. The brown dashed line represents the analytic equation $\rho = (1 - \alpha)\rho_{liq} + \alpha\rho_{vap}$, where ρ_{liq} and ρ_{vap} are taken from experiment. Not shown are data points for the homogeneously stretched region where $\alpha \ll 0.01$. For all but the mW-4 system, the statistical uncertainties are smaller than the symbol size.

of 4.4×10^4, 2.8×10^6, and 1.8×10^5 for experiment and the mW and TIP4P/2005 water models, respectively) and rearranging yields $\alpha = 1 - \rho/\rho_{liq}$ with a slope of $-1/\rho_{liq}$ and an x-intercept of ρ_{liq}. The simulation data in Figure 3 can then be described by replacing ρ_{liq} for the bulk system with a smaller $\rho_{liq,eff}$ for the bubbly phase to account for surface effects. The values of the x-intercepts indicate that $\rho_{liq,eff}$ decreases with decreasing system size and is smaller for the TIP4P/2005 model than the mW model. However, evaluating the data in Figure 3 with a finer lens indicates failure of this simplified analytical equation because (i) there is a noticeable deviation from the linear behavior at smaller α values particularly for the smaller system sizes and (ii) comparison of the data for the mW-4 and TIP4P/2005-8 systems shows a smaller slope but larger intercept for the mW-4 system. Thus, a more microscopic analysis is needed to determine the density of the liquid region for the bubbly water phases. Furthermore, surface effects neglected in the analytic equation may also play a role.

The liquid density in the bubbly water phase can be obtained by fitting the radial shell density profile $\rho(r)$ to a hyperbolic tangent function:

$$\rho(r) = \frac{1}{2}(\rho_{liq,fit} + \rho_{vap,fit}) + \frac{1}{2}(\rho_{liq,fit} - \rho_{vap,fit}) \tanh \frac{2(r - r_0)}{d} \quad (12)$$

where r is the radial distance from the center of mass of the bubble, and r_0 and d are the radial position and thickness of the interface, respectively.[58] This radial analysis assumes a predominantly spherical shape of the bubble, an issue that will be addressed below. The location of the inflection point in the hyperbolic tangent function (r_0) can also be used as an estimate of the bubble radius. The shell density profiles for the mW-32 and TIP4P/2005-4 systems at ρ = 800 kg/m^3 are shown in Figure S5. The radial shell density profiles also allow for an estimation of the fraction of molecules present within the interfacial region

$$\alpha_{int} = \frac{1}{N} \int_{r_0 - d/2}^{r_0 + d/2} 4\pi r^2 \rho(r)\, dr \quad (13)$$

The uncertainties for $\rho_{liq,fit}$, r_0, and α_{int} were estimated as the standard error of the mean at 95% confidence interval from five shell density profiles, each averaged over 200 frames. The numerical values are provided in Tables S2−S15.

Figure 4 depicts $\rho_{liq,fit}$ and α_{int} as a function of system density for all bubbly water phases. At fixed density, as the system size increases, $\rho_{liq,fit}$ is getting closer to the value of the bulk

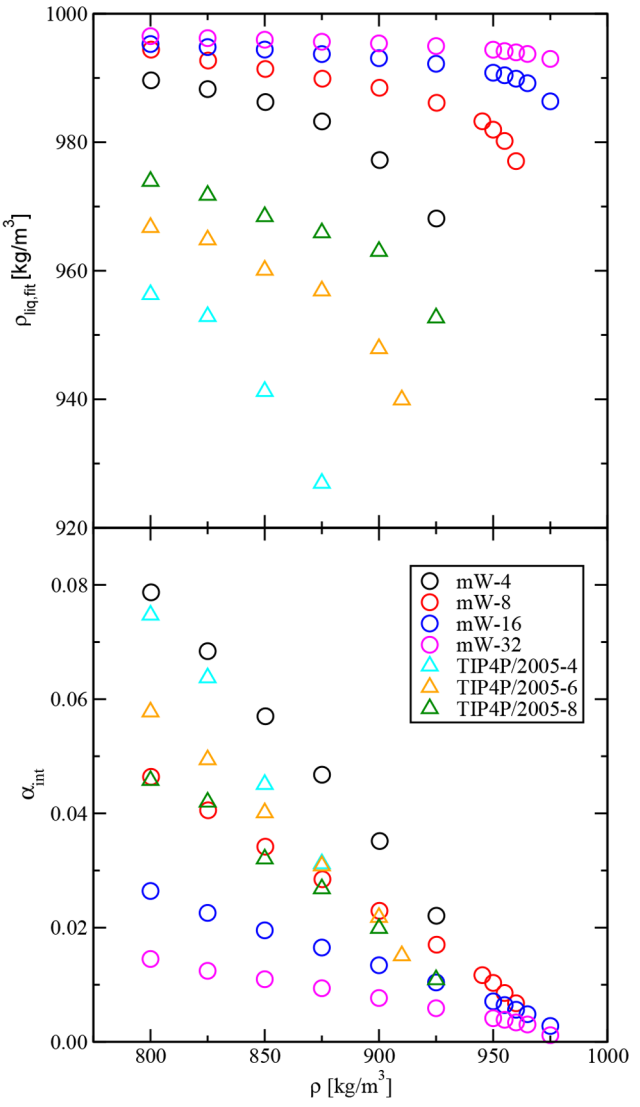

Figure 4. Density of liquid region ($\rho_{liq,fit}$) (top) and fraction of interfacial molecules (α_{int}) (bottom) determined from the radial shell density profile as functions of system density ρ.

DOI: 10.1021/acs.jced.9b00284
J. Chem. Eng. Data 2019, 64, 3755−3771

saturated liquid density. Interestingly, for a given system size and model, $\rho_{liq,fit}$ increases as ρ decreases, but decreasing ρ corresponds to heterogeneous phases with larger bubbles. The values of $\rho_{liq,fit}$ range from 927 kg/m^3 (= 0.932 ρ_{liq}) for TIP4P/2005-4 at ρ = 875 kg/m^3 (smallest system size and ρ closest to the BC point) to 996.5 kg/m^3 (= 0.9988 ρ_{liq}) for mW-32 at ρ = 800 kg/m^3 (largest system size and lowest value of ρ). The differences in $\rho_{liq,fit}$ for the bubbly phases between the two models at the same ρ and system size are much larger than the 3 kg/m^3 difference in ρ_{liq} for the bulk liquid. Since the differences in the bulk vapor−liquid surface tension are also very small, differences in the isothermal compressibility for the stretched liquid and in the ability to accommodate high-curvature interfaces must be responsible for the differences between the mW and TIP4P/2005 models. The fraction of molecules at the interface (see Figure 4) decreases with increasing system size at the same ρ (whereas α increases) because the number of molecules in the liquid region grows much faster than the interfacial area. At the same ρ and system size, the α_{int} values are quite similar (with the exception of the data point for the TIP4P/2005 model closest to the BC point) for the mW and TIP4P/2005 models. Therefore, the differences in $\rho_{liq,fit}$ are mostly responsible for the shift of the α versus ρ lines in Figure 3.

One important question is whether the nanobubbles present in the simulations (ranging in radius from about 0.8 to 11 nm) deviate significantly from a spherical shape due to enhanced fluctuations for such small sizes (compared to bubbles observed in flow experiments, see Figure 1). The dependence of the shape anisotropy factor (κ^2) on system density and size is shown in Figure 5 (and numerical data are provided in Tables S2−S15). The TIP4P/2005-4 and mW-4 simulations

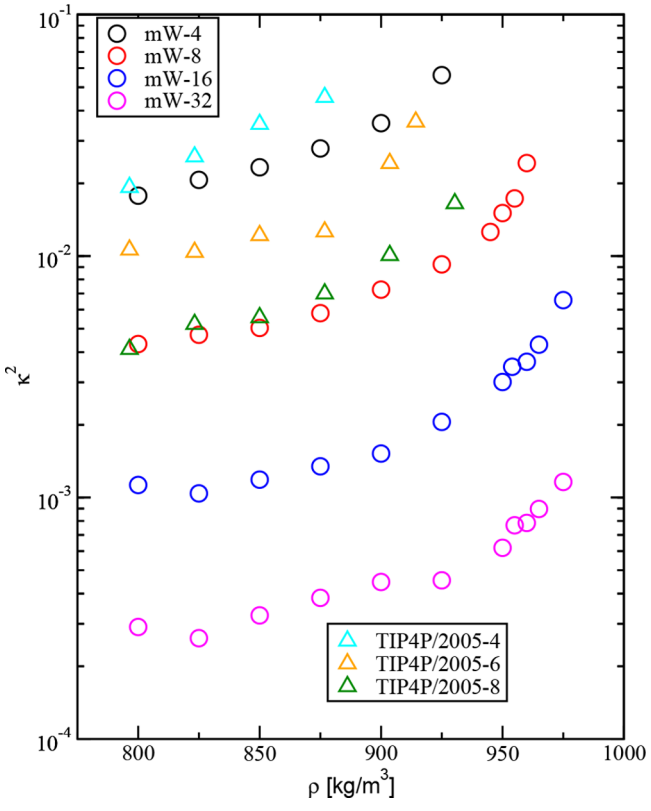

Figure 5. Shape anisotropy factor as a function of system density.

yield the largest κ^2 values, but even here κ^2 is less than 0.06, that is, a very small shape anisotropy. The values for mW-4 and mW-8 at the same density are somewhat smaller than those for TIP4P/2005-4 and TIP4P/2005-8, respectively, but these do not correspond to bubbles of exactly the same size due to the differences in $\rho_{liq,fit}$ between the two models. As the linear dimension of the system increases by a factor of 2, κ^2 decreases by about a factor of 4 at the same density. Thus, in all cases, the bubbles are sufficiently spherical in shape that a sphere radius can also be obtained from $r^* = (3V_{cell}/4\pi)^{1/3}$. The numerical values of r^* are provided in Tables S2−S15. The dependence of κ^2 on r^* is shown in Figure S6. In this case, all data points fall on the same master curve; that is, the dependence on the model is much smaller than on r^*, and the bubble size governs the extent of the shape fluctuations.

Figure S7 shows a comparison of r_0 values obtained from the shell density profiles to the r^* values calculated from the bubble volumes. These data can be well described by a linear fit, $r_0 = kr^* + d$. Irrespective of model and system size, regression coefficients are greater than 0.9999, indicating an exceptional correlation between r_0 and r^*. The slopes for all combinations of model and system size are unity with a maximum deviation of 1% for the TIP4P/2005-4 system. In terms of the offset d, the values for all mW system sizes fall between 0.08 and 0.09 nm. This consistent offset can be explained by the difference in the analysis approaches. The density profiles treat atoms as point particles without any spatial extent. In contrast, the cell method for determining the bubble volume correctly accounts for the volume taken up by the water molecules (excluded volume due to repulsive part of the interaction potential). Hence, we argue that r^* is a better descriptor of the true volume occupied by the bubble and available to vapor or permanent gas molecules, whereas r_0 is a better descriptor of the thermodynamic location of the interface.

Pressure. The virial pressure (P) of the systems versus total density is displayed in Figure 6 (numerical data are provided in Tables S2−S15). The pressure is negative for all systems except for the saturated liquid. Please note that the finite number of molecules used in the canonical-ensemble simulations leads to small variations in the system density (see Tables S2−S15) that cause some scatter in P for $\rho \approx \rho_{liq}$. González et al.[56] have also calculated the pressure of homogeneously stretched liquid water for the TIP4P/2005 water model using NVT simulations (N = 500, T = 296.4 K) and reported values of −187 and −207 MPa at 893 and 878 kg/m^3, respectively. In comparison, our values of −168 and −189 MPa for the TIP4P/2005-4 system at 900 and 885 kg/m^3, respectively, (N = 1925 and 1892, respectively) yield a slightly less negative pressure. Furthermore, our TIP4P/2005-4 simulation at 875 kg/m^3 spontaneously forms a bubbly phase (resulting in an upward jump in pressure), and the larger TIP4P/2005-8 system yields a bubbly phase already at 910 kg/m^3. However, considering differences in the simulation parameters (number of molecules, cutoff distance used for Lennard-Jones interactions, Ewald sum control parameters, and method to constrain the geometry of each molecule), these differences in pressure are not unexpected.

Among all combinations of water model and system size, the qualitative trends for the relationship of system pressure and density are consistent. Comparing the two simulation protocols (decreasing the density starting from a homogeneous phase versus increasing the density starting from a bubbly

DOI: 10.1021/acs.jced.9b00284
J. Chem. Eng. Data 2019, 64, 3755−3771

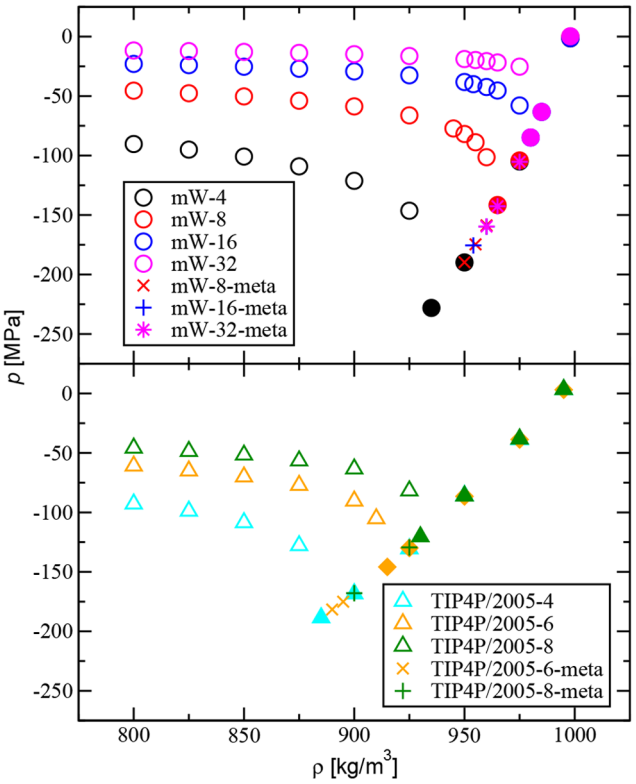

Figure 6. System pressure versus density. Open and filled symbols represent bubbly and homogeneously stretched water systems, respectively. The plusses, crosses, and stars show data for metastable homogeneous systems. Uncertainties are all smaller than the symbol size.

phase), the overall shape of the pressure versus density curve is very similar, but the path of decreasing density allows for a deeper penetration into the homogeneously stretched region and more significant (in magnitude) upward jump of the pressure as the SC point is passed than the downward jump in pressure as the BC point is passed. For convenience, the discussion here and also for the other thermophysical properties starts with the path of decreasing density from ρ_{sat} to 800 kg/m^3 (protocol 1), then turns to the path of increasing density from 800 kg/m^3 to ρ_{sat} (protocol 2).

The data in Figure 6 show that, as the system density is decreased from the saturated liquid density, the pressure initially decreases approximately linearly to very large negative values. Comparing the behavior of the pressure for the mW and TIP4P/2005 systems at the same system size, it is apparent that the rate at which P decreases with decreasing ρ in the homogeneously stretched region, the SC density, and the maximum tension that the system can sustain before cavitation are all three smaller in magnitude for the TIP4P/2005 model than for the mW model. After passing the SC point, P jumps upward to a much less negative value, and then enters a region where it slowly increases with decreasing density (increasing bubble volume), but always remains negative. The negative pressure signals that the system could lower its energy through a decrease in the system volume ($P = -(\partial U/\partial V)_T$) that would lead to disappearance of the bubble and less stretching for the homogeneous phase, but, of course, the volume of the simulation box is constrained in the canonical ensemble (as is also the cell volume in most CFD simulations).

While the values of P in the homogeneously stretched state at a given ρ do not depend significantly on system size, there is a clear system-size dependence for P in the bubbly water region where larger systems yield less negative values of P at the same ρ (see Figure 6). However, the density of the liquid region of the bubbly phase itself depends on system size (see Figure 4). When P is plotted as a function of $\rho_{liq,fit}$ for the bubbly systems instead of ρ, then the data for the homogeneously stretched phases and the bubbly systems fall onto the same curve (see Figure S8). On the basis of the current molecular simulation data (see Figure 6), we surmise that the use of two separate equations of state covering homogeneously stretched and bubbly phases should be explored for homogeneous mixture models.

It should be noted that, at the same ρ, a larger system contains a larger bubble than a smaller system when both are in the bubbly region. To further investigate the system size dependence, the simulation data were analyzed based on the Young−Laplace equation, which describes the relationship between pressure inside the bubble (P_{in}) and pressure outside the bubble (P_{out}) based on mechanical equilibrium for two-phase fluids:

$$P_{in} - P_{out} = \frac{2\gamma^*}{R} \tag{14}$$

where γ^* and R are the surface tension and the bubble radius, respectively, that is taken here as r^*. Since the saturated vapor pressure predicted by both water models is a very small positive number at T = 298 K, we assume that P_{in} is negligible and that P_{out} can be set equal to the system pressure ($-P \approx 2\gamma^*/r^*$). For the bubbly region, the negative of the system pressure P is plotted against the reciprocal of the bubble radius r^* in Figure 7. As an aside, we again note that the radius of the smallest bubble oberved for the system density just below the BC point is found to increase with increasing system size. Regardless of system size, the correlation between $-P$ and $1/r^*$ is close to linear for both water models with a correlation coefficient of R^2 larger than 0.995. Therefore, we can conclude that even at the sub-10 nm scale, the Young−Laplace equation is still applicable within some small tolerance, which is consistent with the findings of some previous studies.[59,60] However, when the surface tension value γ^* is estimated by applying the Young−Laplace equation to each individual data point, then a trend emerges where γ^* increases nearly linearly with decreasing inverse bubble radius for both the mW and TIP4P/2005 models (see Figure 7). Thus, formation of the convex liquid−vapor surface results in a smaller free energy penalty than for the planar surface. The slope of γ^* versus $1/r^*$, a metric for the curvature effect, is more negative for the TIP4P/2005 model than for the mW model. The smaller curvature effect for the mW model may explain why this model can sustain a larger maximum tension before cavitation becomes spontaneous.

Using an unweighted linear fit to estimate the value of γ^* at zero curvature ($1/r^* = 0$) yields 65.3 ± 0.2 and 66.9 ± 0.2 mN/m for the TIP4P/2005 and mW models, respectively. For the TIP4P/2005 model, this value agrees within uncertainties with the separate calculation of γ for the planar interface (see Table 2), whereas the extrapolation for the mW model yields a value that is about 2% larger than γ.

Potential Energy. The system potential energy U is plotted as a function of density in Figure 8 (numerical data are provided in Tables S2−S15). The TIP4P/2005 model yields

DOI: 10.1021/acs.jced.9b00284
J. Chem. Eng. Data 2019, 64, 3755−3771

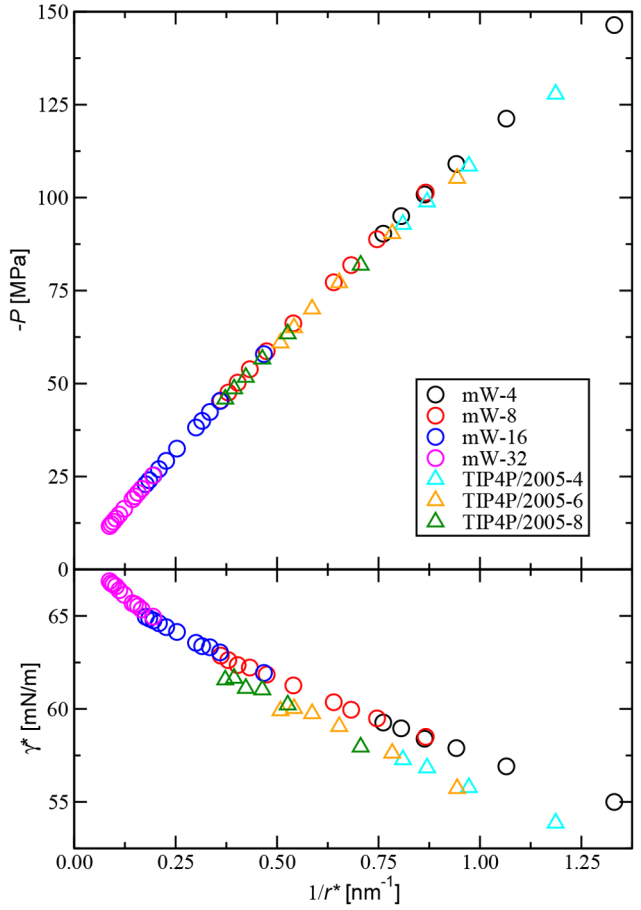

Figure 7. Negative system pressure (top) and bubble surface tension (bottom) versus inverse bubble radius. Data points are collected from all bubbly water phases for all combinations of water models and system sizes. Statistical uncertainties are smaller than the symbol size.

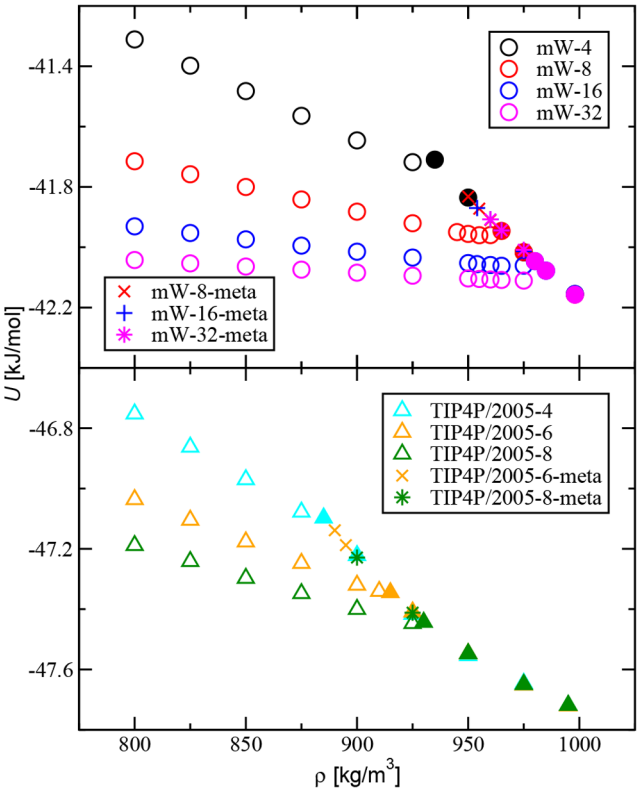

Figure 8. System potential energy versus density. Open and filled symbols represent bubbly and homogeneously stretched water systems, respectively. The plusses, crosses, and stars show data for metastable homogeneous systems. Uncertainties are all smaller than the symbol size.

an overestimation of ΔH_{vap} and, hence, U is shifted downward compared to the mW model. In the homogeneously stretched region, the potential energy increases with decreasing density (consistent with the negative pressure, see Figure 6) and the magnitude of the slope is greater for the mW model (consistent with its more negative value of P compared to the TIP4P/2005 model at the same ρ and system size). For both water models, U exhibits a downward jump when cavitation occurs from the metastable phase because the favorable decrease of the potential energy of the less-stretched liquid region outweighs the energetic cost of forming a highly curved interface. The slower increase in U as density decreases results from a competition due to the favorable increase of the density of the liquid region and the unfavorable increase in the fraction of interfacial molecules (see Figure 4), and it is consistent with the smaller magnitude of the negative pressure.

Residual Isochoric Heat Capacity. The density dependence of the residual isochoric heat capacity $C_{V,res}$ is shown in Figure 9 (numerical data are provided in Tables S2−S15). $C_{V,ideal}$ for water at 300 K is around 27.3 J/(K·mol) as estimated from the molecular partition function in a previous work.[61] The experimental C_V for bulk liquid water at ambient conditions is 74.5 J/(mol·K).[62] After incorporating the contribution from $C_{V,ideal}$, the TIP4P/2005 water model overestimates C_V by around 20%, while the mW water model underestimates C_V by around 35%.

Among all combinations of model and system size, the qualitative changes in $C_{V,res}$ with ρ are consistent. $C_{V,res}$ initially increases when approaching the SC point from the saturated liquid phase. When cavitation occurs, $C_{V,res}$ drops and then enters a flat region where the change does not exceed the statistical uncertainties. However, in all cases, $C_{V,res}$ in the two-phase region remains larger than that of the saturated liquid phase. The observation that $C_{V,res}$ initially increases when approaching the transition point is consistent with previous findings,[63,64] indicating growing energy fluctuations as the system is being stretched. The decrease of $C_{V,res}$ when cavitation occurs indicates that the system undergoes a relaxation. The relatively larger value of $C_{V,res}$ for the bubbly region compared with that for the saturated liquid phase indicates that the presence of an interface introduces additional energy fluctuations into the system. However, the density of the liquid region $\rho_{liq,fit}$ in the bubbly systems is smaller than that of ρ_{liq} at saturation (i.e., the liquid region is stretched), and this certainly also contributes to the larger value of $C_{V,res}$.

$C_{V,res}$ values for the bubbly water systems exhibit a system size dependence as well. Although going from mW-32 to mW-16 and TIP4P/2005-8 to TIP4P/2005-6 at a given ρ, the $C_{V,res}$ values overlap within uncertainties but, with one exception, the values for the smaller system are always larger. A further decrease of box length yields a larger increase in $C_{V,res}$. These findings indicate that fluctuations are more pronounced for smaller system sizes (larger values of α_{int}).

Shear Viscosity. The shear viscosity η as a function of system density is shown in Figure 10 (numerical data are

DOI: 10.1021/acs.jced.9b00284
J. Chem. Eng. Data 2019, 64, 3755−3771

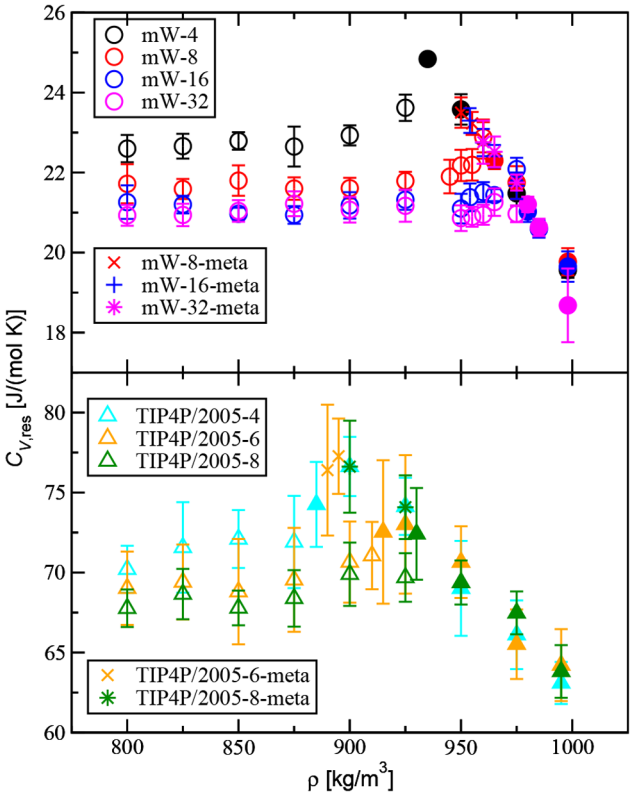

Figure 9. System residual isochoric heat capacity versus density. Open and filled symbols represent bubbly and homogeneously stretched water systems, respectively. The plusses, crosses, and stars show data for metastable homogeneous systems.

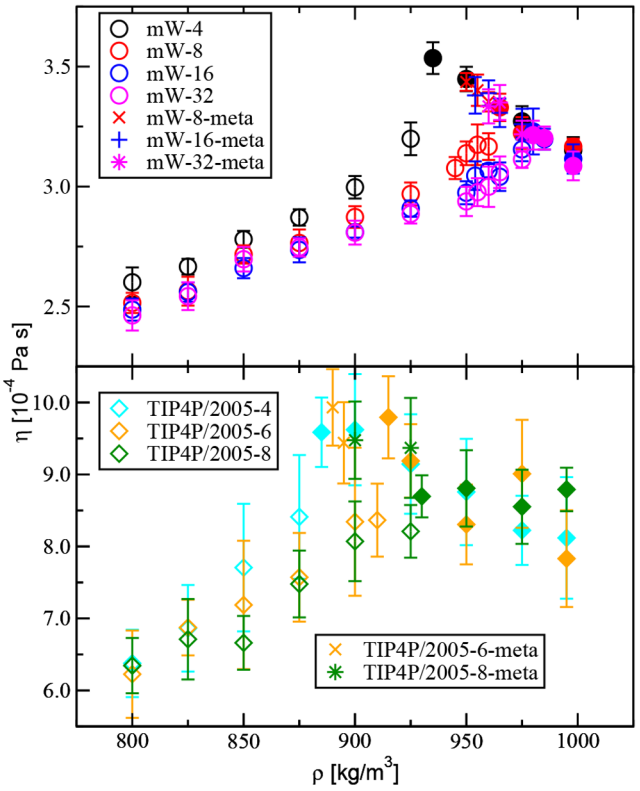

Figure 10. Shear viscosity versus density. Open and filled symbols represent bubbly and homogeneously stretched water systems, respectively. The plusses, crosses, and stars show data for metastable homogeneous systems.

provided in Tables S2−S15). The shear viscosities predicted by the mW and TIP4P/2005 water models for the saturated liquid phase agree well with that from previous simulations,[54,65] and the corresponding experimental value is 8.90 × 10^{-4} Pa·s.[62] In terms of accuracy, the TIP4P/2005 model underestimates η by less than 10%, whereas the mW model underestimates η by a factor of 2.9. This significant underestimation can likely be attributed to a faster momentum transfer through long-range collisions without the need to reorient dipole−dipole vectors and break hydrogen bonds for the case of the mW model.

For the mW model, the shear viscosity is found to initially increase when approaching the SC point. The value at the SC point is approximately 12% larger than that of the saturated liquid phase for the mW-4 system. When cavitation occurs, η jumps down and then enters a region where it decreases approximately linearly with decreasing system density. Dhabal et al.[65] have previously studied liquid-state anomalies of water using the mW model, and they also observed an increase of η when ρ decreases from bulk liquid density to 960 kg/m^3 at T = 300 K. Due to the larger relative uncertainites for the TIP4P/2005 systems, the initial increase in η as the density decreases in the homogeneously stretched region is less evident. For the TIP4P/2005-4 system, η at ρ = 885 kg/m^3 is about 20% larger than for the saturated liquid. De Hijes et al.[66] have also calculated the shear viscosity of liquid water for the TIP4P/2005 model at T = 300 K and N = 216, and they reported an initial increase and then decrease when ρ decreases from bulk liquid density to 800 kg/m^3, with a local maximum near 880 kg/m^3. The initial increase is consistent with our data, but since our smallest system size ($N \approx 2000$) only allows for water to stay homogeneous with density values larger than 875 kg/m^3, the local maximum was not detected clearly in this work.

For the two-phase region, the slope in η versus ρ is larger for the TIP4P/2005 model than for the mW model, and there appears to be a system size dependence for η as well. However, predicted values for the two largest systems for both water models agree with each other within uncertainties. Since an analytic equation that correlates η and ρ could potentially be useful for predicting multiphase flow in CFD, and the TIP4P/2005 model is much more accurate than the mW model for predicting shear viscosity, the data for the TIP4P/2005-8 system were fitted to a linear equation: $\eta/(\text{Pa·s}) = (0.0163 \times 10^{-4}\ \text{m}^3/\text{kg})\rho - 6.7732 \times 10^{-4}$, with a correlation coefficient of R^2 = 0.93. Some of the analytic equations used in current multiphase CFD simulations[17] correlate the viscosity of the bubbly water phase as a function of the bubble volume fraction (which itself is a linear function of ρ, see Figure 3) and, hence, the shear viscosity is plotted versus bubble volume fraction in Figure 11. In this case, all data points fall onto a straight line[67] for a given water model. Thus, the dependence of η on system size for a given ρ is caused by the dependence of the bubble volume fraction on system size. Using the data from the TIP4P/2005 systems, the linear equation $\eta/(\text{Pa·s}) = (-17.463 \times 10^{-4})\alpha + 8.8596 \times 10^{-4}$ (with R^2 = 0.93) is obtained, where the intercept agrees well with the value of $(8.82 \pm 0.38) \times 10^{-4}$ Pa·s found for the TIP4P/2005-8 system at saturation.

Beyond the simple linear relation, a more complex relation between two-phase viscosity and bubble volume fraction was

DOI: 10.1021/acs.jced.9b00284
J. Chem. Eng. Data 2019, 64, 3755−3771

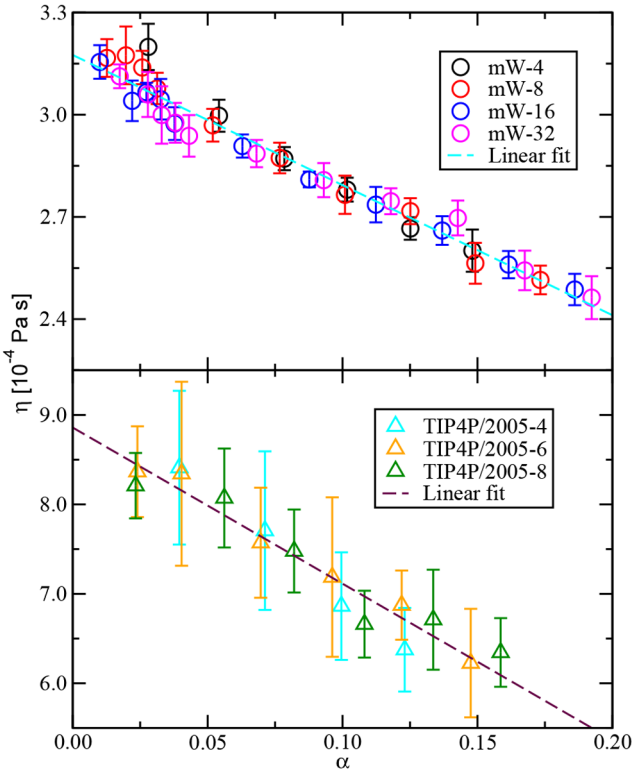

Figure 11. Shear viscosity versus bubble volume fraction.

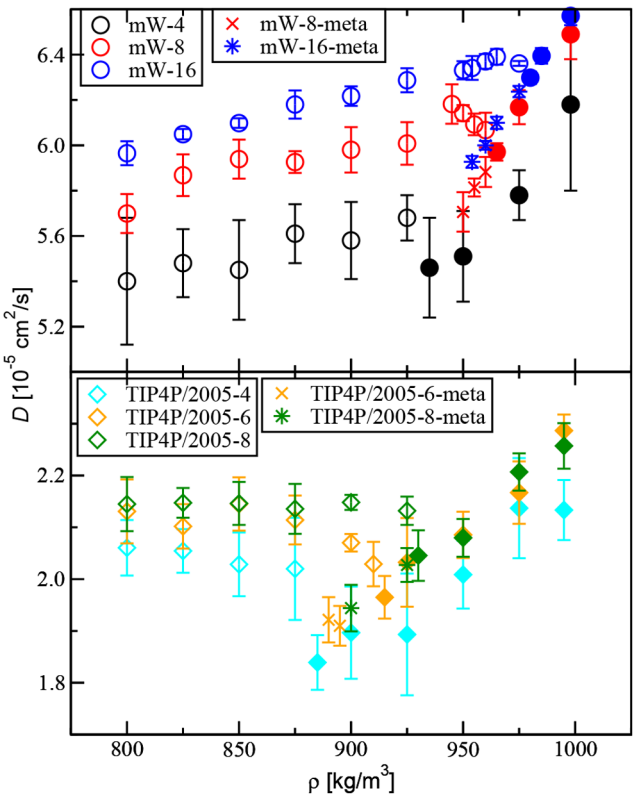

Figure 12. Self-diffusion coefficient versus density. Open and filled symbols represent bubbly and homogeneously stretched water systems, respectively. The plusses, crosses, and stars show data for metastable homogeneous systems.

proposed by Beattie and Whalley:[68] $\eta = \alpha\eta_{vapor} + (1 - \alpha)(1 + 2.5\alpha)\eta_{liq}$, where the term $(1 + 2.5\alpha)$ follows theoretical arguments.[69] The quadratic dependence yields an initial increase in η with increasing α for small α values. The data for bubbly phases presented in Figure 11 do not show an initial increase, but we also do not observe infinitely small bubbles due to the transition to the homogeneously stretched phase at the BC density. On the other hand, the data including the homogeneously stretched phase show an initial increase with decreasing density (see Figure 10). Indeed the size of the transient voids in the homogeneously stretched regime is of molecular dimensions (<0.1 nm^3). On the basis of the current molecular simulation data (see Figure 10), we surmise that use of two separate linear regimes covering homogeneously stretched and bubbly phases should be explored to describe the dependence of the viscosity on density and direction of the density change.

Self-Diffusion. The self-diffusion coefficient D_{self} as a function of density is shown in Figure 12 (numerical data are provided in Tables S2−S15). Previous studies have shown that diffusion coefficients calculated from molecular dynamics simulations depend on system size, and corrections have been proposed to estimate the thermodynamic limit of D_{self}.[70,71] However, in practice, many studies prefer to use a sufficiently large system instead of a correction, and it has been shown to mitigate the system size effect of water at ambient conditions.[72,73] Since system size effects are of interest for the current paper, a correction for the diffusion coefficient was not used here. The diffusion coefficient for the saturated liquid phase obtained for the mW-16 system is $(6.57 \pm 0.04) \times 10^{-5}$ cm^2/s, which is in excellent agreement with 6.5×10^{-5} cm^2/s from a previous study.[28] The calculated value for the saturated liquid phase of the TIP4P/2005-8 system ($N = 17023$) is $(2.26 \pm 0.04) \times 10^{-5}$ cm^2/s, which is significantly larger than the value of 2.06×10^{-5} cm^2/s reported previously for $N = 360$.[54,74] The experimental diffusion coefficient for liquid water at 298 K and saturation is 2.30×10^{-5} cm^2/s.[75] Our calculated value from TIP4P/2005-8 simulation underestimates the experimental value by less than 2% and finite-size corrections or simulations for larger systems may further reduce this deviation. In contrast, the mW-16 simulations yield a D_{self} that is too large by a factor of 2.9, which is consistent with the predicted shear viscosity of saturated liquid water assuming the Stokes−Einstein relation.

Regardless of the system size and water model, the diffusion coefficient initially decreases when approaching the spinodal point from the saturated liquid phase. The reason for this anomalous behavior of water is that, as the density decreases, a larger fraction of the water molecules populates low-density states that are dynamically less mobile because a less-strained tetrahedral network leads to a higher activation barrier for transport.[66] When cavitation occurs, D_{self} jumps to a larger value. A further decrease in the density leads to a statistically significant decrease in D_{self} for the mW-8 and mW-16 systems, but no significant change was observed for the mW-4 and all TIP4P/2005 systems. Although the relative uncertainties are larger for the TIP4P/2005 systems (likely because of its slower, but more accurate diffusion), there is no indication that the data supports a decrease in D_{self} with decreasing ρ in the bubbly region. As indicated in Figure 12, D_{self} increases with system size irrespective of the system being homogeneously stretched or in the two-phase region, but the relative increase appears to be larger for the two-phase region. For the homogeneously stretched systems, the diffusion coefficients

DOI: 10.1021/acs.jced.9b00284
J. Chem. Eng. Data 2019, 64, 3755−3771

seem to reach a satisfactory level of convergence in terms of system size going from mW-8 to mW-16 and TIP4P/2005-6 and TIP4P/2005-8, while convergence in terms of system size is not achieved for the two-phase systems.

For both water models, D_{self} for the bubbly region is smaller than for the saturated liquid phase. A likely explanation for this behavior is that the activation barrier for evaporation is much larger than the activation barrier for diffusion and, hence, the molecules in the liquid region must follow a more tortuous diffusion pathway around the bubble.[76] Furthermore, the fact that η is also found to be smaller for the bubbly region indicates that the Stokes−Einstein relation does not hold for the bubbly region. Figure S9 shows D_{self} as a function of η^{-1}; within statistical uncertainties, the behavior of the homogeneously stretched systems (including the metastable states) follows the Stokes−Einstein relation with D_{self} increasing linearly with increasing η^{-1}. However, the Stokes−Einstein relation breaks down for the bubbly region. For the mW model, D_{self} is found to decrease with increasing η^{-1}, and D_{self} appears to be independent of η^{-1} for the TIP4P/2005 model. The deviations from the Stokes−Einstein relation in the bubbly region are much more pronounced than the previously observed deviations for the homogeneously stretched region.[66]

CONCLUSION

For all combinations of water models and system sizes studied in this work, the canonical ensemble simulations at T = 298 K yield a homogeneously stretched phase for $\rho \geq 980$ kg/m^3 and a bubbly state (with a spherical vapor bubble surrounded by a liquid region) for $\rho \leq 875$ kg/m^3. For the intermediate density region, the outcome of the simulations depends on the simulation protocol and system size. For simulations started from a homogeneous configuration, the homogeneously stretched state persists to lower densities until reaching a spinodal cavitation (SC) point where bubble formation is spontaneous (or requires passing a readily surmounted free energy barrier). In contrast, for simulations started from a state with a preformed spherical cavity, the bubbly state persists to densities higher than the SC point until a bubble collapse (BC) point is reached when the system spontaneously converts to a homogeneously stretched state. This behavior is akin to the hysteresis loop well-known for adsorption−desorption isotherms in mesoporous materials. As the system size is increased, both SC and BC points occur at larger densities. Extrapolation versus inverse simulation box length yields infinite-size estimates of 912 ± 14 and 961 ± 3 kg/m^3 for the spinodal densities of the TIP4P/2005 and mW models, respectively.

When the water system is still in the homogeneously stretched state (including the metastable part of the hysteresis loop), then system size effects are not significant with the exception of the diffusion coefficient. For the inhomogeneous bubbly water region, system size effects (comparing properties for the same ρ and T, but different N and V) are observed for all properties. The main reason for these pronounced system size effects is that, at the same ρ and T, a larger system contains a larger bubble than the smaller system, and some properties (e.g., pressure, density of the liquid region, and shape anisotropy of the bubble) are described better as a function of bubble radius instead of bubble volume fraction. On the other hand, the viscosity of the two-phase system is well described as a function of the bubble volume fraction, the isochoric heat capacity for bubbly systems does not show a strong dependence on bubble radius nor volume fraction.

Qualitatively similar trends are observed for the thermophysical properties obtained for the TIP4P/2005 and mW water models with the exception of D_{self} in the bubbly region. As the density is decreased from the saturated liquid density, the pressure decreases to a large negative value ($P < -100$ MPa near the SC point for both models), the magnitude of the potential energy decreases by only about 1%, whereas the residual isochoric heat capacity and viscosity increase by more than 10%, and the self-diffusion coefficient decreases by more than 10%. Upon cavitation, the system undergoes a relaxation as signaled by steep and sudden changes in these properties. A further decrease in the density (increase in bubble volume fraction and radius) leads to a relatively slower increase in P and U, a decrease in η, and a decrease in D_{self} for the mW model, but not the TIP4P/2005 model, whereas $C_{V,res}$ exhibits no significant changes. Upon bubble collapse, the discontinuous changes in properties follow the reverse trend (i.e., opposite sign) as those encountered at the SC point, but are much smaller in magnitude.

Given that the mW and TIP4P/2005 water models yield the same qualitative trends for the various thermophysical properties (except for the diffusion coefficient in the bubbly region) studied in this work, we surmise that the mW water model, albeit coarse-grained and much less accurate than the TIP4P/2005 model, remains a good choice for the qualitative study of bubbly water systems at ambient conditions and allows to access much larger system sizes and longer time scales. However, when quantitative predictions are of concern, then the TIP4P/2005 water model is preferable, but, without polarization correction, there are significant deviations for the saturated vapor pressure and heat of vaporization.

The pressure of bubbly water systems is well described by the Young−Laplace equation, but both water models exhibit a decrease in the effective surface tension with increasing curvature. Interestingly, the simulations show that many properties in the two-phase region cannot be obtained from an interpolation of the properties of the saturated liquid and vapor phases. The value of the residual isochoric heat capacity, which depends on fluctuations of the system potential energy, is larger for the bubbly water phase than for the saturated liquid phase (and of course also the saturated vapor phase), whereas the self-diffusion coefficient is smaller for the bubbly region than for the saturated liquid phase (and of course also the saturated vapor phase) due to molecules having to diffuse around the bubble. The viscosity is largest for the homogeneously stretched phase near the SC point, and the Stokes−Einstein relation is not obeyed in the bubbly region.

The results of this work can inform multiphase flow CFD studies. Most importantly, although a negative pressure is not considered possible in most present CFD simulations because of the use of an EOS valid only in the thermodynamic limit, a negative pressure is observed here for both homogeneously stretched liquid water and bubbly water. The Young−Laplace equation can be utilized to estimate the negative pressure of bubbly water systems from the bubble radius that, in turn, can be deduced from the CFD cell density and length. Furthermore, some recent experimental studies have also investigated the EOS for water under negative pressure.[77,78] Using extensive simulation data for the TIP4P/2005 water model, Biddle et al.[79] have proposed an extension of the two-structure EOS for water that covers a pressure range from large

DOI: 10.1021/acs.jced.9b00284
J. Chem. Eng. Data 2019, 64, 3755−3771

negative to large positive values and incorporates the spinodal. In general, we have to keep in mind that under a turbulent cavitating flow condition, both the pressure range and temperature range might be large inside the flow domain. Thus, a proper choice of EOS to describe liquid water is already a posing challenge, not to mention the challenge of describing the two-phase region. In the homogeneously stretched and bubbly regions, as discussed above, values of some of the thermophysical properties fall outside the range spanned by the corresponding values for the saturated vapor and liquid properties; an observation that precludes estimating these properties based on interpolation between the thermodynamically stable phases. In addition, due to the pronounced hysteresis loop, some properties are path dependent. Thus, changes in the analytic equations underlying CFD simulations of multiphase flow may need to be considered.

■ ASSOCIATED CONTENT

Supporting Information

The Supporting Information is available free of charge on the ACS Publications website at DOI: 10.1021/acs.jced.9b00284.

Supplementary figures and tables providing system size information and the numerical data obtained from the simulations (PDF)

■ AUTHOR INFORMATION

Corresponding Author

*E-mail: siepmann@umn.edu.

ORCID

J. Ilja Siepmann: 0000-0003-2534-4507

Notes

The authors declare no competing financial interest.

■ ACKNOWLEDGMENTS

This work is supported by the United States Office of Naval Research under Grant ONR N00014-17-1-2676 with Dr. Ki-Han Kim as the program manager. Part of the computer resources was provided by the Minnesota Supercomputing Institute.

■ REFERENCES

(1) Suslick, K. S. Sonochemistry. *Science* **1990**, *247*, 1439−1445.

(2) Crowe, C. T. *Multiphase Flow Handbook*; CRC Press: Boca Raton, FL, 2005.

(3) Yadigaroglu, G.; Hewitt, G. F. *Introduction to Multiphase Flow: Basic Concepts, Applications and Modelling*; Springer: Cham, CH, 2017.

(4) Russell, P. S.; Giosio, D. R.; Venning, J. A.; Pearce, B. W.; Brandner, P. A.; Ceccio, S. Microbubble Generation from Condensation and Turbulent Breakup of Sheet Cavitation. 31st Symposium on Naval Hydrodynamics, Monterey, CA, 2016.

(5) Binder, K.; Block, B. J.; Virnau, P.; Tröster, A. Beyond the van der Waals Loop: What can be Learned from Simulating Lennard-Jones Fluids inside the Region of Phase Coexistence. *Am. J. Phys.* **2012**, *80*, 1099−1109.

(6) Thommes, M.; Kaneko, K.; Neimark, A. V.; Olivier, J. P.; Rodriguez-Reinoso, F.; Rouquerol, J.; Sing, K. W. Physisorption of Gases, with Special Reference to the Evaluation of Surface Area and Pore Size Distribution (IUPAC Technical Report). *Pure Appl. Chem.* **2015**, *87*, 1051−1069.

(7) Abascal, J. L. F.; González, M. A.; Aragones, J. L.; Valeriani, C. Homogeneous Bubble Nucleation in Water at Negative Pressure: A Voronoi Polyhedra Analysis. *J. Chem. Phys.* **2013**, *138*, 084508.

(8) González, M. A.; Menzl, G.; Aragones, J. L.; Geiger, P.; Caupin, F.; Abascal, J. L. F.; Dellago, C.; Valeriani, C. Detecting Vapour Bubbles in Simulations of Metastable Water. *J. Chem. Phys.* **2014**, *141*, 18C511.

(9) Menzl, G.; Gonzalez, M. A.; Geiger, P.; Caupin, F.; Abascal, J. L. F.; Valeriani, C.; Dellago, C. Molecular Mechanism for Cavitation in Water under Tension. *Proc. Natl. Acad. Sci. U. S. A.* **2016**, *113*, 13582−13587.

(10) Niedźwiedzka, A.; Schnerr, G. H.; Sobieski, W. Review of Numerical Models of Cavitating Flows with the Use of the Homogeneous Approach. *Arch. Thermodyn.* **2016**, *37*, 71−88.

(11) Goncalves, E.; Patella, R. F. Numerical Simulation of Cavitating Flows with Homogeneous Models. *Comput. Fluids* **2009**, *38*, 1682−1696.

(12) Gnanaskandan, A.; Mahesh, K. A Numerical Method to Simulate Turbulent Cavitating Flows. *Int. J. Multiphase Flow* **2015**, *70*, 22−34.

(13) Shin, B. R.; Iwata, Y.; Ikohagi, T. Numerical Simulation of Unsteady Cavitating Flows Using a Homogeneous Equilibrium Model. *Comput. Mech.* **2003**, *30*, 388−395.

(14) Kieffer, S. W. Sound Speed in Liquid-Gas Mixtures: Water-Air and Water-Steam. *J. Geophys. Res.* **1977**, *82*, 2895−2904.

(15) Pokusaev, B. G.; Tairov, E. A.; Vasilyev, S. A. Low Frequency Pressure Waves in a Vapor-Liquid Medium with a Fixed Layer of Spherical Particles. *Acoust. Phys.* **2010**, *56*, 306−312.

(16) Awad, M. M.; Muzychka, Y. S. Effective Property Models for Homogeneous Two-Phase Flows. *Exp. Therm. Fluid Sci.* **2008**, *33*, 106−113.

(17) Aung, N. Z.; Yuwono, T. Evaluation of Mixture Viscosity Models in the Prediction of Two-Phase Flow Pressure Drops. *ASEAN J. Sci. Technol. Dev.* **2012**, *29*, 115−128.

(18) Ruocco, G.; Sampoli, M.; Torcini, A.; Vallauri, R. Molecular Dynamics Results for Stretched Water. *J. Chem. Phys.* **1993**, *99*, 8095−8104.

(19) Netz, P. A.; Starr, F. W.; Stanley, H. E.; Barbosa, M. C. Static and Dynamic Properties of Stretched Water. *J. Chem. Phys.* **2001**, *115*, 344−348.

(20) Netz, P. A.; Starr, F.; Barbosa, M. C.; Stanley, H. E. Computer Simulation of Dynamical Anomalies in Stretched Water. *Braz. J. Phys.* **2004**, *34*, 24−31.

(21) Stanley, H. E.; Barbosa, M. C.; Mossa, S.; Netz, P. A.; Sciortino, F.; Starr, F. W.; Yamada, M. Statistical Physics and Liquid Water at Negative Pressures. *Phys. A* **2002**, *315*, 281−289.

(22) Abascal, J. L. F.; Vega, C. A General Purpose Model for the Condensed Phase of Water: TIP4P/2005. *J. Chem. Phys.* **2005**, *123*, 234505.

(23) Ewald, P. Die Berechnung Optischer und Elektrostatischer Gitterpotentiale. *Ann. Phys.* **1921**, *369*, 253−287.

(24) Allen, M. P.; Tildesley, D. J. *Computer Simulation of Liquids*; Oxford University Press: Oxford, UK, 1987.

(25) Hockney, R. W.; James, W. E. *Computer Simulation Using Particles*; CRC Press: Boca Raton, FL, 1988.

(26) Sadus, R. J. *Molecular Simulation of Fluids*; Elsevier Science: Amsterdam, NL, 1999.

(27) Frenkel, D.; Smit, B. *Understanding Molecular Simulation: From Algorithm to Applications*; Elsevier Science: San Diego, CA, 2001.

(28) Molinero, V.; Moore, E. B. Water Modeled As an Intermediate Element between Carbon and Silicon. *J. Phys. Chem. B* **2009**, *113*, 4008−4016.

(29) Panagiotopoulos, A. Z. Direct Determination of Phase Coexistence Properties of Fluids by Monte Carlo Simulation in a New Ensemble. *Mol. Phys.* **1987**, *61*, 813−826.

(30) Panagiotopoulos, A. Z.; Quirke, N.; Stapleton, M.; Tildesley, D. J. Phase Equilibria by Simulation in the Gibbs Ensemble: Alternative Derivation, Generalization and Application to Mixture and Membrane Equilibria. *Mol. Phys.* **1988**, *63*, 527−545.

(31) Siepmann, J. I.; Martin, M. G.; Chen, B.; Wick, C. D.; Stubbs, J. M.; Potoff, J. J.; Eggimann, B. L.; McGrath, M. J.; Zhao, X. S.;

DOI: 10.1021/acs.jced.9b00284
J. Chem. Eng. Data 2019, 64, 3755−3771

Anderson, K. E. et al. *Monte Carlo for Complex Chemical Systems-Minnesota*, version 16.1; Minneapolis, MN. 2016.
(32) Metropolis, N.; Rosenbluth, A. W.; Rosenbluth, M. N.; Teller, A. H.; Teller, E. Equation of State Calculations by Fast Computing Machines. *J. Chem. Phys.* **1953**, *21*, 1087−1092.
(33) Barker, J. A.; Watts, R. O. Structure of Water: A Monte Carlo Calculation. *Chem. Phys. Lett.* **1969**, *3*, 144−145.
(34) Siepmann, J. I.; Frenkel, D. Configurational Bias Monte Carlo: A New Sampling Scheme for Flexible Chains. *Mol. Phys.* **1992**, *75*, 59−70.
(35) Vlugt, T. J. H.; Martin, M. G.; Smit, B.; Siepmann, J. I.; Krishna, R. Improving the Efficiency of the Configurational-Bias Monte Carlo Algorithm. *Mol. Phys.* **1998**, *94*, 727−733.
(36) Bai, P.; Siepmann, J. I. Assessment and optimization of configurational-bias Monte Carlo particle swap strategies for simulations of water in the Gibbs ensemble. *J. Chem. Theory Comput.* **2017**, *13*, 431−440.
(37) Plimpton, S. Fast Parallel Algorithms for Short-Range Molecular Dynamics. *J. Comput. Phys.* **1995**, *117*, 1−19.
(38) Hoover, W. G. Canonical Dynamics: Equilibrium Phase-Space Distributions. *Phys. Rev. A: At., Mol., Opt. Phys.* **1985**, *31*, 1695−1697.
(39) Ryckaert, J.-P.; Ciccotti, G.; Berendsen, H. J. C. Numerical Integration of the Cartesian Equations of Motion of a System with Constraints: Molecular Dynamics of *n*-Alkanes. *J. Comput. Phys.* **1977**, *23*, 327−341.
(40) Kirkwood, J. G.; Buff, F. P. The Statistical Mechanical Theory of Surface Tension. *J. Chem. Phys.* **1949**, *17*, 338−343.
(41) Martínez, L.; Andrade, R.; Birgin, E. G.; Martínez, J. PACKMOL: A Package for Building Initial Configurations for Molecular Dynamics Simulations. *J. Comput. Chem.* **2009**, *30*, 2157−2164.
(42) Martínez, J.; Martínez, L. Packing Optimization for Automated Generation of Complex System's Initial Configurations for Molecular Dynamics and Docking. *J. Comput. Chem.* **2003**, *24*, 819−825.
(43) Stillinger, F. H., Jr Rigorous Basis of the Frenkel-Band Theory of Association Equilibrium. *J. Chem. Phys.* **1963**, *38*, 1486−1494.
(44) Arkin, H.; Janke, W. Gyration Tensor Based Analysis of the Shapes of Polymer Chains in an Attractive Spherical Cage. *J. Chem. Phys.* **2013**, *138*, 054904.
(45) Tsai, D. H. The Virial Theorem and Stress Calculation in Molecular Dynamics. *J. Chem. Phys.* **1979**, *70*, 1375−1382.
(46) Thompson, A. P.; Plimpton, S. J.; Mattson, W. General Formulation of Pressure and Stress Tensor for Arbitrary Many-body Interaction Potentials under Periodic Boundary Conditions. *J. Chem. Phys.* **2009**, *131*, 154107.
(47) Smith, J. M.; Van Ness, H. C.; Abbott, M. M. *Introduction to chemical engineering thermodynamics*; McGraw-Hill: Boston, MA, 2005.
(48) McQuarrie, D. A. *Statistical Mechanics*; University Science Books: Sausalito, CA, 2004.
(49) Kubo, R. Statistical-Mechanical Theory of Irreversible Processes. I. General Theory and Simple Applications to Magnetic and Conduction Problems. *J. Phys. Soc. Jpn.* **1957**, *12*, 570−586.
(50) Petravic, J.; Harrowell, P. Linear Response Theory for Thermal Conductivity and Viscosity in terms of Boundary Fluctuations. *Phys. Rev. E* **2005**, *71*, 061201.
(51) Zhang, Y.; Otani, A.; Maginn, E. J. Reliable Viscosity Calculation from Equilibrium Molecular Dynamics Simulations: A Time Decomposition Method. *J. Chem. Theory Comput.* **2015**, *11*, 3537−3546.
(52) NIST Chemistry Webbook: Water. https://webbook.nist.gov/cgi/cbook.cgi?ID=7732185 (accessed Nov. 28,2018).
(53) Vega, C.; De Miguel, E. Surface Tension of the Most Popular Models of Water by Using the Test-Area Simulation Method. *J. Chem. Phys.* **2007**, *126*, 154707.
(54) Vega, C.; Abascal, J. L. F. Simulating Water with Rigid Non-Polarizable Models: A General Perspective. *Phys. Chem. Chem. Phys.* **2011**, *13*, 19663−19688.
(55) Factorovich, M. H.; Molinero, V.; Scherlis, D. A Simple Grand Canonical Approach to Compute the Vapor Pressure of Bulk and Finite Size Systems. *J. Chem. Phys.* **2014**, *140*, 064111.
(56) González, M. A.; Valeriani, C.; Caupin, F.; Abascal, J. L. F. A Comprehensive Scenario of the Thermodynamics Anomalies of Water Using the TIP4P/2005 Model. *J. Chem. Phys.* **2016**, *145*, 054505.
(57) Debenedetti, P. G. *Metastable liquids: concepts and principles*; Princeton University Press: Princeton, NJ, 1996.
(58) Cahn, J. W.; Hilliard, J. E. Free Energy of a Nonuniform System. I. Interfacial Free Energy. *J. Chem. Phys.* **1958**, *28*, 258−267.
(59) Matsumoto, M.; Tanaka, K. Nano Bubble—Size Dependence of Surface Tension and inside Pressure. *Fluid Dyn. Res.* **2008**, *40*, 546.
(60) Yan, H.; Wei, J.; Cui, S.; Xu, S.; Sun, Z.; Zhu, R. On the Applicability of Young-Laplace Equation for Nanoscale Liquid Drops. *Russ. J. Phys. Chem. A* **2016**, *90*, 635−640.
(61) Furtenbacher, T.; Szidarovszky, T.; Hrubỳ, J.; Kyuberis, A. A.; Zobov, N. F.; Polyansky, O. L.; Tennyson, J.; Császár, A. G. Definitive Ideal-Gas Thermochemical Functions of the $H_2{}^{16}O$ Molecule. *J. Phys. Chem. Ref. Data* **2016**, *45*, 043104.
(62) Haynes, W. M. *CRC Handbook of Chemistry and Physics*; CRC Press: Boca Raton, FL, 2014.
(63) Baidakov, V. G.; Protsenko, S. P.; Kozlova, Z. R. The Isochoric Heat Capacity of a Metastable Lennard-Jones Fluid. *Chem. Phys. Lett.* **2007**, *447*, 236−240.
(64) Altabet, Y. E.; Singh, R. S.; Stillinger, F. H.; Debenedetti, P. G. Thermodynamic Anomalies in Stretched Water. *Langmuir* **2017**, *33*, 11771−11778.
(65) Dhabal, D.; Chakravarty, C.; Molinero, V.; Kashyap, H. K. Comparison of Liquid-State Anomalies in Stillinger-Weber Models of Water, Silicon, and Germanium. *J. Chem. Phys.* **2016**, *145*, 214502.
(66) de Hijes, P. M.; Sanz, E.; Joly, L.; Valeriani, C.; Caupin, F. Viscosity and Self-Diffusion of Supercooled and Stretched Water from Molecular Dynamics Simulations. *J. Chem. Phys.* **2018**, *149*, 094503.
(67) Dukler, A. E.; Wicks, M.; Cleveland, R. G. Frictional Pressure Drop in Two-phase Flow.Part B: An Approach Through Similarity Analysis. *AIChE J.* **1964**, *10*, 44−51.
(68) Beattie, D. R. H.; Whalley, P. B. A Simple Two-Phase Frictional Pressure Drop Calculation Method. *Int. J. Multiphase Flow* **1982**, *8*, 83−87.
(69) Einstein, A. Berichtigung zu Meiner Arbeit: "Eine Neue Bestimmung der Moleküldimensionen. *Ann. Phys.* **1911**, *339*, 591−592.
(70) Yeh, I. C.; Hummer, G. System-Size Dependence of Diffusion Coefficients and Viscosities from Molecular Dynamics Simulations with Periodic Boundary Conditions. *J. Phys. Chem. B* **2004**, *108*, 15873−15879.
(71) Heyes, D. M.; Cass, M. J.; Powles, J. G.; Evans, W. A. B. Self-Diffusion Coefficient of the Hard-Sphere Fluid: System Size Dependence and Empirical Correlations. *J. Phys. Chem. B* **2007**, *111*, 1455−1464.
(72) Zeebe, R. E. On the Molecular Diffusion Coefficients of Dissolved CO_2, HCO_3^-, and CO_3^{2-} and Their Dependence on Isotopic Mass. *Geochim. Cosmochim. Acta* **2011**, *75*, 2483−2498.
(73) Guevara-Carrion, G.; Vrabec, J.; Hasse, H. Prediction of Self-Diffusion Coefficient and Shear Viscosity of Water and its Binary Mixtures with Methanol and Ethanol by Molecular Simulation. *J. Chem. Phys.* **2011**, *134*, 074508.
(74) Vega, C.; Abascal, J. L. F.; Conde, M. M.; Aragones, J. L. What Ice Can Teach Us About Water Interactions: A Critical Comparison of the Performance of Different Water Models. *Faraday Discuss.* **2009**, *141*, 251−276.
(75) Krynicki, K.; Green, C. D.; Sawyer, D. W. Pressure and Temperature Dependence of Self-Diffusion in Water. *Faraday Discuss. Chem. Soc.* **1978**, *66*, 199−208.
(76) Bai, P.; Haldoupis, E.; Dauenhauer, P. J.; Tsapatsis, M.; Siepmann, J. I. Understanding Diffusion in Hierarchical Zeolites with House-of-cards Nanosheets. *ACS Nano* **2016**, *10*, 7612−7618.

DOI: 10.1021/acs.jced.9b00284
J. Chem. Eng. Data 2019, 64, 3755−3771

(77) Davitt, K.; Rolley, E.; Caupin, F.; Arvengas, A.; Balibar, S. Equation of State of Water Under Negative Pressure. *J. Chem. Phys.* **2010**, *133*, 174507.
(78) Caupin, F.; Arvengas, A.; Davitt, K.; Azouzi, M. E. M.; Shmulovich, K. I.; Ramboz, C.; Sessoms, D. A.; Stroock, A. D. Exploring Water and Other Liquids at Negative Pressure. *J. Phys.: Condens. Matter* **2012**, *24*, 284110.
(79) Biddle, J. W.; Singh, R. S.; Sparano, E. M.; Ricci, F.; González, M. A.; Valeriani, C.; Abascal, J. L. F.; Debenedetti, P. G.; Anisimov, M. A.; Caupin, F. Two-structure Thermodynamics for the TIP4P/2005 Model of Water Covering Supercooled and Deeply Stretched Regions. *J. Chem. Phys.* **2017**, *146*, 034502.

DOI: 10.1021/acs.jced.9b00284
J. Chem. Eng. Data 2019, 64, 3755−3771